MEERKAT-BASED MULTI-WAVELENGTH STUDY OF SUPERNOVA REMNANT SN386 (G7.7-3.7)

MWANIKI PATRICK NJOROGE

A Thesis Submitted in Partial Fulfilment of Requirements for Conferment of the Degree of Master of Science in Physics of Meru University of Science and Technology

2025

DECLARATION

This thesis is my original work and has not been presented for a degree in any other Institution

Mwaniki Patrick Njoroge

SC409/201523/21

Signature: Date:

Declaration By Supervisors

This thesis has been presented with our authority as University Supervisors

Dr. Dismas S. Wamalwa, PhD

Meru University of Science and Technology, Kenya

Signature: Date:

Prof. James O. Chibueze, PhD

University of South Africa, South Africa

Signature: Date:

Dr. Dickson M. Kinyua, PhD

Kirinyaga University, Kirinyaga, Kenya

Signature: Date:

ACKNOWLEDGEMENT

I extend my deepest gratitude to my supervisors, Dr. Dismas S. Wamalwa, Prof. James O. Chibueze, and Dr. Dickson M. Kinyua, for their invaluable guidance, support, and dedication throughout this work.

I sincerely acknowledge the Department of Physical Sciences, Meru University of Science and Technology, for their material support in this research.

Additionally, I am grateful to the South African Radio Astronomy Observatory (SARAO), the Inter-University Institute for Data Intensive Astronomy (IDIA), the National Radio Astronomy Observatory (NRAO), XMM-Newton, and the Isaac Newton Telescope (INT) for providing the MeerKAT, computing facility, Very Large Array (VLA), X-ray, and optical data used in this study.

TABLE OF CONTENTS

LIST OF FIGURES

LIST OF APPENDICES

LIST OF ABBREVIATIONS AND SYMBOLS

The following list describes several abbreviations, acronyms, and symbols used.

α	Spectra index
$\dot{\theta}$	Expansion Rate
ν	Shock Seed
Σ	Surface Brightness
θ	Angular Radius
S	Flux Density
d	Distance to Remnant
m	Expansion Parameter
r	Shock Radius
t	Age
CASA	Common Astronomy Software Applications
FITS	Flexible Image Transport System
IAU	International Astronomical Union
INT	Isaac Newton Telescope
ISM	Interstellar Medium
MeerKAT	Meer Karoo Array Telescope
MFS	Multiple-frequency Synthesis
MOST	Molonglo Observatory Synthesis Telescope
MS	Measurement Set
OBSID	Observation ID
RMS	Roort-Mean-Square
SDSS	Sloan Digital Sky Survey
SKA	Square Kilometre Array
SN	Supernova
SNR	Supernova Remnant
VLA	Very Large Array
WFC	Wide Field Camera
XMM	X-ray Multi-Mirror Mission

ABSTRACT

Supernova remnant SN386 (G7.7-3.7) presented captivating attention for multi-wavelength observation. In this study, we investigated the structural characteristics of G7.7-3.7 with higher resolution MeerKAT observation at 1284 MHz, revealing intricate details of its morphology and emission mechanisms. MeerKAT observations revealed G7.7-3.7 as an almost circular structure with filamentary features, manifesting in various blowouts. The western boundary exhibited a strong bright blowout, while the southern perimeter showcased extended bright filaments with feather-like structures, seemingly disconnected from the western blowout. Moreover, the eastern region presented a faint blowout with a centralized bright point source, while faint elongated filaments traversed the northwest, linked the eastern point source and western blowout and progressed outward uniformly. Spectral index analysis indicated a steep spectrum (α ranged $\sim$ 0 to $\sim$ -3), suggesting a combination of synchrotron and few traces of thermal emissions at the edges of bright blowouts. Bright blowouts with a less steep spectrum ranging from $\sim$ -0.5 to $\sim$ -1.5 were dominated by shock-accelerated particles encountering irregularities and weakening in magnetic fields. Spectral index values close to $\alpha = 0$, showed the presence of traces of thermal emissions from shock-heated gases, especially at the edge of the bright blowout. However, the faint emissions along the filaments connecting the eastern and western blowouts with a very steep spectral index of $\sim$ -3 comprised synchrotron emissions from aged particles that had dissipated energy due to turbulent re-acceleration. Analysis of MeerKAT and VLA data gave an expansion of $\Delta\theta$ = 9 ± 0.45 arcsec over a period of Δt = 31.907 yr corresponding to an expansion rate $\dot{\theta}$ = 0.282 ± 0.014 arcsec yr^{-1} . The data recorded a shock speed of 5883 ± 294 km s^{-1} and an age of 1636 ± 115 years. The revised age fitted with the explosion event of 386 CE and the observed data in 2023. Furthermore, our multi-wavelength investigation unveiled an intriguing structure within the southern radio blowout exhibiting a convergence of features such as the bright radio blowout, a prominent X-ray arc and two faint optical filaments aligned with the X-ray bright arc. We attributed the bright radio blowouts to the non-uniform mass outflow from the localized high-density population of the shock-accelerated particles and the weakening of magnetic fields along its perimeter. Thermal emissions traces along the edges of blowouts resulted from shock-heated gases intensifying in the south due to the presence of high-density ISM. Thus, we proposed that the supernova of G7.7-3.7 occurred in an environment of varying densities of interstellar medium (ISM). Consequently, this environment facilitated X-ray emissions and the formation of faint optical filaments due to collisions with the ISM and the circumstellar materials from the progenitor star respectively. Our findings shed light on the complex interplay of physical processes within G7.7-3.7, offering valuable insights into the dynamics and evolution of supernova remnants.

CHAPTER ONE: INTRODUCTION

1.1 Introduction

Supernova remnants (SNRs) are formed from massive stars undergoing explosive supernova events caused by catastrophic gravitational collapse (Cotton et al., 2024b; Domček et al., 2023; Dubner, 2008). These events, among the most energetic in the universe, Zhou et al. (2018), leave behind expanding shells of gas and dust that can be observed across multiple wavelengths (Dubner & Giacani, 2015). In this work, our interest is centered on SN386 (G7.7-3.7) which is located within the Nan-Dou asterism (Stephenson & Green, 2002).

The study of SNRs provides valuable insights into the life cycles of stars, the mechanisms of supernova explosions, and their impact on the surrounding interstellar medium (ISM) (Dubner et al., 1996; Dubner & Giacani, 2015; Green, 2015; Leahy et al., 2022; Vink, 2020). In a Type II supernova, this process can result in the formation of a neutron star or black hole. The explosion generates a powerful shockwave that propagates through the ISM, compressing and heating it while accelerating particles to relativistic speeds. These high-energy particles interact with magnetic fields, producing synchrotron radiation observable in multiple wavelengths. As the remnant expands, it gradually cools and slows, developing complex filamentary structures influenced by interactions with the surrounding medium. Over time, the supernova remnant enriches the ISM with heavy elements such as oxygen, iron, and silicon, contributing to the formation of future stars and planetary systems. SNRs also offer a unique opportunity to investigate the acceleration of cosmic rays, Domček et al. (2023) and Vink (2020), and the properties of magnetic fields in the Milky Way galaxy (Dubner et al., 1996; Dubner & Giacani, 2015).

G7.7-3.7 (PKS 1814-24) was initially documented as a radio source in early catalogs during the 1960s, bearing the catalog number PKS 1814-24 (Gardner et al., 1969). This subtle, diffuse radio source is located at ~ ($18^h17^m25^s$, -24°04′) B1950 (Cotton et al., 2024b; Dubner et al., 1996; Green, 2014, 2019). It was initially reported as a supernova remnant (SNR) by Milne and Dickel (1974b). In recent studies, Zhou et al. (2018) proposed that G7.7-3.7 could potentially be linked to the supernova event of 386 CE (SN386); one of the rare instances of historical SNRs resulting from a supernova with extremely low luminosity. This unique characteristic could make G7.7-3.7 particularly valuable for studying the evolution and origin of this specific supernova (Domček et al., 2023).

Nevertheless, investigating supernova remnants (SNRs) presents its fair share of difficulties. One of the primary hurdles is the precise determination of their age, distance, and size (Green, 2015). Understanding these factors is crucial for analyzing their evolutionary stages and placing them within a historical framework associated with their explosive events. In the specific instance of SN386 (G7.7-3.7), the ambiguity surrounding its age and distance persists due to the scarcity of extensive research and observational data (Domček et al., 2023; Zhou et al., 2018).

Nonetheless, only a limited number of studies have delved into the characteristics of G7.7-3.7 within the radio spectrum. The initial investigation, conducted by Gardner et al. (1969), identified it as a radio source and noted a substantial linear polarization of $\approx$ 10 % of the total intensity. This finding was corroborated by subsequent radio analyses by Milne and Dickel (1975) and Dubner et al. (1996). Its radio morphological structure shows a nearly circular shell structure, marked by an unresolved peak feature situated in the eastern region (Dickel & Milne, 1976; Dubner et al., 1996; Green, 2014; Milne, 1987; Milne & Dickel, 1974a, 1975; Milne & Dickel, 1974b; Milne et al., 1986). Additionally, it exhibits extensive

and conspicuous bright regions that extend along its southern and western boundaries, as illustrated in Figure 2.3.

The size of G7.7-3.7 extends across a diameter of $\sim 22'$ (Dubner et al., 1996; Green, 2014, 2019; Milne & Dickel, 1974a; Milne et al., 1986). Its spectral index, α, is approximately -0.32, indicating a relatively flat and uniform spectrum across the entire source (Dubner et al., 1996; Gardner et al., 1969; Green, 2014, 2019; Milne et al., 1986). However, there is a noticeable steepening, ($\alpha \sim -0.6$) (see Figure 2.5), observed in regions of high emissivity to the west (Dubner et al., 1996; Milne et al., 1986).

In the study by Dubner et al. (1996), the surface brightness, Σ, at a frequency of 1 GHz was calculated using the formula $\Sigma_{1GHz} = 1.5 \times 10^{-19}(S/\theta^2)$ W m^{-2} Hz^{-1} sr^{-1}, where S represents the flux density at 1 GHz and is determined by interpolating data from the tabulated spectral index and found that $\Sigma_{1GHz} \simeq 3.5 \times 10^{-21}$ W m^{-2} Hz^{-1} sr^{-1}. According to Milne et al. (1986) findings, it was suggested that the distance to G7.7-3.7 is $\sim 3.2 - 6$ kpc. This estimation was derived based on the Σ–D (radio surface brightness–diameter) relation, which provides a rough measure of the distance to the object (Dubner, 2016; Dubner & Giacani, 2015; Green, 2015). At the observed frequency, the mean linearly polarized intensity of G7.7-3.7 accounts for roughly 10% of the total intensity (Dubner et al., 1996; Gardner et al., 1969; Milne & Dickel, 1975; Milne et al., 1986). Dubner et al. (1996) noted a partial alignment of polarized radiation with the western portion of the shell and the filament connecting the east and west, even though polarization angles were not consistently oriented, as in Figure 2.6. Importantly, areas with the highest total intensity lacked polarization distribution (see Figure 2.7) (Dubner et al., 1996).

Recent radio studies by Cotton et al. (2024b) resolved most of the shells into many very

faint thin filaments in MeerKAT image of G7.7-3.7 at a resolution of 10″ at 1335 MHz (See Figure 2.4). The integrated flux density was S_{1335} = 5.2 ± 0.40 Jy and an average diameter of about 27′ which indicated large-scale emission filtered out by the interferometer. There was a strong filamentary structure with significant polarization and its "B" vectors, representing the projected orientation of the magnetic field, were primarily aligned with the filaments. Faraday rotation gradients were steep, with north-west values being the largest (see Figure 2.8). The faint blowouts along its perimeter consist mainly of mass outflows suggesting that they may have resulted from the weakening magnetic field at that place.

Very few investigations have been conducted on G7.7-3.7 in other spectral regions. In the case of gamma-ray (γ-ray) observations, Acero et al. (2016), there was no detection of an SNR associated with this source. In the mid-IR spectrum, there are three regions with significant warm dust emission near the outer edge of the radio-emitting shell. These regions have temperatures between 50 to 100 K according to thermal models. The most prominent one is at the core of a planetary nebula within G7.7-3.7's field of view, the second corresponds to a radio feature with a steep spectrum in the west, and the third lies just outside the radio shell to the south-east (Arendt, 1989; Domček et al., 2023; Milne et al., 1986).

In an X-ray study as shown in Figure2.9, G7.7-3.7 was found to have an X-ray arc-like feature in the south and a point-like source in the north-east (Smith, 2010; Zhou et al., 2018). Zhou et al. (2018), focused on the X-ray arc-like feature in the south, suggesting that the plasma's age is $\sim$ 1.2 ± 0.6 kyrs, with subsolar abundances, signifying a shocked interstellar medium. In optical observations, van den Bergh (1978) noted the visibility of G7.7-3.7 in the optical spectrum. A recent study by Domček et al. (2023) found faint optical emission in the southern part of the SNR, featuring two east-west-oriented optical filaments

(see Figure 2.11) that align with the X-ray emitting region (see Figure 2.10) (Smith, 2010; Zhou et al., 2018). The study suggests that these optical filaments are likely formed due to the SNR colliding with a dense circumstellar shell in the southern region.

However, probing the secrets of SNRs like SN386 presents considerable challenges, notably in precisely determining their age, distance, shock speed and size. The age and distance of SN386 remain elusive, largely due to the limited depth of previous research and observational data. A paucity of comprehensive multi-wavelength studies has hindered a holistic understanding of this enigmatic remnant. This work describes analysis of the MeerKAT observation of G7.7-3.7 at a resolution of $5''.7$ in L-band. Compared MeerKAT data with previous radio data from VLA to constrain the age of G7.7-3.7. Finally, combined MeerKAT data with X-ray and optical data to analyze the multiwavelength structure of G7.7-3.7.

1.2 Statement of the Problem

Supernova remnant G7.7-3.7 presents a complex and intriguing astrophysical puzzle. Existing limited studies in various spectral domains, including radio, X-ray, IR, optical, and γ-ray, have offered fragmented insights into this object, leaving crucial questions unanswered such as age and shock speed. G7.7-3.7 has intrigued astronomers for years due to its uncertain age, distance, and the enigmatic nature of the underlying supernova blowout (Cotton et al., 2024b; Domček et al., 2023; Zhou et al., 2018). While historical records suggest an association with a low-luminosity supernova event in 386 CE, Zhou et al. (2018), critical details remain elusive. Current multi-wavelength observations of G7.7-3.7 have limitations in accurately determining its age, distance, and physical properties, as well as a comprehensive understanding of its nature and interactions with its environment (Green, 2015). These limitations hinder a comprehensive understanding of this cosmic object and

its historical significance. The absence of a unified, multi-wavelength study of G7.7-3.7 limits a holistic perspective on this intriguing supernova remnant.

However, recent advancements in radio astronomy, particularly the MeerKAT radio telescope, offer a powerful tool for conducting a multi-wavelength study of G7.7-3.7. MeerKAT's unique capabilities and high sensitivity provide an opportunity to address these knowledge gaps comprehensively. A multi-wavelength investigation of G7.7-3.7 utilizing MeerKAT higher resolution radio observation enables the study of the evolution of spectral index and structural analysis of G7.7-3.7, sheds light on the nature of the underlying supernova event, and offers insights into its interactions with the surrounding environment.

1.3 General Objective of the Study

To conduct a comprehensive multi-wavelength investigation of SNR386 (G7.7-3.7) using the MeerKAT higher-resolution radio observations to study its evolution and structural analysis.

1.3.1 Specific Objectives of the Study

1. Analyze higher resolution radio structure of G7.7-3.7 at L band.
2. Investigate the resolved spectral index structure of G7.7-3.7 at the L band.
3. Analyze the multiwavelength structure of G7.7-3.7.
4. Discuss how G7.7-3.7 interacts with the ISM.

1.4 Justification of the Study

The research on Supernova Remnant G7.7-3.7 is scientifically and historically significant. Understanding this celestial object can provide insights into supernova remnants and the historical context of stellar explosions. This research enhances our understanding of mas-

sive star life cycles, their explosive deaths, and interactions with the interstellar medium. MeerKAT's advanced capabilities make it an ideal tool for this investigation, with implications extending beyond astrophysics.

CHAPTER TWO: LITERATURE REVIEW

2.1 Introduction to Supernova Remnants (SNRs)

Supernovae (SNe) explosion, the most energetic processes in the universe, marks the death of massive and supermassive stars that exhausted all their nuclear fuels (Hirashima et al., 2023; Michailidis et al., 2024; Vasiliev & Shchekinov, 2024). The SNe explosion releases approximately 10^{51} ergs of mechanical energy, irreversibly altering the physical and chemical properties of large regions within galaxies (Dubner & Giacani, 2015; Giacani, 2017; Hirashima et al., 2023; Mantovanini et al., 2024; Reyes-Iturbide et al., 2024; Romano et al., 2024).

Additionally, about tens of solar masses are ejected to the interstellar medium (ISM) (Dubner & Giacani, 2015; Kirchschlager et al., 2024; Zhou et al., 2024). During SNe explosion, the outward propagating shock wave blows off the star's outer layers in different directions such that a large portion of the stellar envelope is ejected at velocities between ~5 000 and 20 000 km s^{-1} (Dubner & Giacani, 2015). This high SNe expansion velocity distinguishes SNe outburst from nebulosity. The ejected materials are slowed down by ambient ISM thousands or hundred years later and the velocity decreases greatly to even hundreds or tens of km s^{-1}. Eventually, they disperse and mix with the surrounding clouds or gases (Dubner & Giacani, 2015; Zhou et al., 2024). The interaction product between the ejecta of a SNe explosion and the surrounding circumstellar and ISM forms a complex stellar structure after the explosion which constitutes SNR (Arias et al., 2024; Giacani, 2017; Kirchschlager et al., 2024; Kochanek et al., 2024). While SNe explosion occurs in a small duration observable within a few years of the occurrence, their remnant can be observed for several thousands to millions of years.

SNRs are visible evidence of interactions between the ejected materials during the SNe explosions and the surrounding circumstellar and ISM (Arias et al., 2024; Giacani, 2017; Kochanek et al., 2024; Kopsacheili et al., 2024; Long, 2017; Winkler et al., 2023). SNRs are compact regions of ionized gas excited by a shock wave interacting with the ISM (Reyes-Iturbide et al., 2024). These SNR regions radiate across the entire electromagnetic spectrum from radio wavelengths to gamma rays (Giacani, 2017; Long, 2017). SNRs play a critical role in the chemical evolution of galaxies and ISM via their enrichment with heavy elements and contribution to new star formation (Kopsacheili et al., 2024; Sano et al., 2023). The investigation of SNRs across the entire electromagnetic spectrum indicates they are the primary source of Galactic cosmic rays and serve as essential tests for particle acceleration in astrophysical shock studies (Case & Bhattacharya, 1996; Duvidovich et al., 2017; Giacani, 2017; Sinitsyna & Sinitsyna, 2024; Tu et al., 2024).

The morphological structure of SNRs is influenced by various local and external factors (Long, 2017). Local factors include the types of SNe explosion, pulsar presence or absence, elapsed time since SNe explosion, progenitors history of mass loss, earlier SNR presence or absence and the surrounding ISM density and complexity (Arias et al., 2024; Mantovanini et al., 2024). The external factors comprising the line of sight absorption amount and distance to SNR further contribute to the observed SNRs properties. SNR observations revealed different morphological features including clumps, shells, filaments, lobes and ears (protrusions from the remnant) (Arias et al., 2024; Reyes-Iturbide et al., 2024; Soker, 2023).

Advancement in radio astronomy was very significant to SNRs study and a number of the Milky Way bright sources were grouped as SNRs (Mantovanini et al., 2024; Winkler et al., 2023). Radio observations played a crucial role in providing insights into the evolution of

the SNRs (Dubner & Giacani, 2015). They can also give information about the structure, strength and orientation of the magnetic field of the SNRs (Shanahan et al., 2023). Polarization observations of the SNRs in radio bands can provide the geometry and orientation of the magnetic fields within the SNRs (Cotton et al., 2024a; Pavlović et al., 2018). The radio emission polarization of SNRs can offer information on the diffusion and transport of cosmic rays within them (Dubner & Giacani, 2015). Generally, radio observations of SNRs play a critical role in studying the dynamics, magnetic fields, particle acceleration and their evolutions (Cotton et al., 2024a; Shanahan et al., 2023). However, decades ago, SNRs were discovered beyond radio wavelength (Long, 2017; Sinitsyna & Sinitsyna, 2024). Combining X-ray, optical, IR, and radio observations of SNRs provides insights to gain a complete or complex structure of SNRs (Fesen et al., 2024; Kopsacheili et al., 2024; Long, 2017; Mantovanini et al., 2024; Zhou et al., 2024).

2.2 Existing Observations of G7.7-3.7

Few observations of G7.7-3.7 have been conducted in radio, X-ray and opical.

2.2.1 Radio Observations of G7.7-3.7

Comprehensive observation of G7.7-3.7 was initially conducted by Milne et al. (1986) with 843 MHz Molonglo Observatory Synthesis Telescope (MOST) and with Parkes Radio Telescope at 8.4 GHz. After synthesis for 12 hrs, MOST had a synthesized beam of $44'' \times 108''$ and the observation was made. The observation field was far from the galactic plane for the map to be free of artifacts caused by sources outside the field of view. The total CLEANed flux density was 7 Jy and the CLEAN image was a contour map in Figure 2.1.

In 64-m Parkes radio telescope observation at 8.4 GHz, the cooled FED receiver had a single channel of 200 MHz bandwidth, 80 K system temperature and $3'$ half-power beamwidth.

The total power and the modulated component were detected when the receiver was switched between orthogonal linear polarizations. The primary flux calibrator was Hydra A (8.2 Jy) and the instrumental polarization was checked against the Orion nebula and Hydra A. Detailed observations and methods of data reduction are described in Milne and Dickel (1974a, 1975) and Milne et al. (1986). The generated map and polarization E-vectors of the field observed are shown in Figure 2.2.

Dubner et al. (1996) carried out radio observation of G7.7-3.7 using Very Large Array (VLA) DnC configuration at 1.465 GHz with 50 MHz bandwidth. The mosaicing technique was used as its size was larger than half a primary beam at the observed frequency. Five fields of G7.7-3.7 were observed and combined into a single image in the u-v plane using tasks of the experimental software system SDE. The integration time was 21 minutes per field. The primary flux density and phase calibrator was 3C 286 under the assumption that G7.7-3.7 has a flux density of 14.7 Jy at 1.4 GHz. The size of the synthesized beam was $70'' \times 35''$ at a position angle of 6 degrees. The rms noise of the final image was 1.5 mJy/beam. Single-dish data was added to the mosaic to recover the short spatial frequency information. This single-dish observation was conducted with the 30 m antenna of the Instituto Argentino de Radioastronomia (IAR). The IAR observation was calibrated using Hydra A under the assumption that G7.7-3.7 has a flux density of S = 43.2 Jy at 1.42 GHz. The resulting VLA + IAR image of G7.7-3.7 is shown in Figure 2.3.

Recently Cotton et al. (2024b) presented full stokes MeerKAT *L*-band (856 - 1712 MHz) observation of G7.7-3.7 at 1.3 GHz. A detailed description of MeerKAT is described by Jonas and MeerKAT Team (2016) and Mauch et al., 2020. The exposure time was 2.1 hours with a total session time including calibration of 9.5 hours. A higher-spectral-resolution polarization analysis was done. Further details about the MeerKAT observation of G7.7-

3.7, data analysis and imaging are described in Cotton et al. (2024b). The MeerKAT image of G7.7-3.7 is shown in Figure 2.4.

2.2.2 X-ray Observation of G7.7-3.7

Zhou et al. (2018) described in details the X-ray observation of G7.7-3.7. In 2005 and 2012, G7.7-3.7 was observed with *XMM-Newton* by E. Gotthelf (OBSID: 0304220401) and M. Smith (OBSID: 0671170101) respectively (Zhou et al., 2018). In the 2012 observation, the pn and MOS cameras, that were operating in full frame with a thin filter, covered the whole G7.7-3.7. However, the 2005 observation was targeted to the nearby point source AX J1817.6-2401 where pn/MOS cameras were in full frame/small window mode with a medium filter. The X-ray emitting region was fully covered by the MOS2 camera at an off-axis region while partially in MOS1 and missed by the pn camera. Thus, X-ray imaging of G7.7-3.7 was done using all MOS and pn data in 2012 and only MOS2 data in 2005. The screened exposure time in 2005 MOS2 data was only 2.9 ks while in 2012 was 7.5, 6.6 and 6.3 ks for MOS1, MOS2 and pn respectively. The *XMM-Newton* data was reduced and analyzed as described by Zhou et al. (2018) to produce an image shown in Figure 2.9.

2.2.3 Optical Observation of G7.7-3.7

In Domček et al. (2023), G7.7-3.7 was observed using the Wide Field Camera (WFC) instrument at the prime focus of the 2.5 m Isaac Newton Telescope (INT) on August 2019 and 2022. The detector had a field-of-view $\sim 34' \times 34'$ with $0.33''$ pix^{-1}. In the 2019 observation, the narrow-band filters Hα + [NII], Hβ, [OIII] and [SII] were used to obtain the data. The SDSS broad-band filters r$'$ and g$'$ were used for continuum subtraction. In the 2022 observation, the data set was expanded with extra observations of Hβ and g$'$ filters. THELI software was used for data reduction as described in Domček et al. (2023). Flux calibration was also performed to obtain the continuum subtracted images.

2.3 Radio Morphology of G7.7-3.7

The MOST intensity contours of the CLEANed radio map of G7.7-3.7 at 843 MHz (see Figure 2.1) shows an almost complete circular shell with a diameter ~20′ at a resolution of 44″ EW × 108″ NS. Bright features marked A and B in Figure 2.1 are in the south-west part of the shell. On the north-west side, there appear to be double shells. In the lower resolution Parkes map of 3′ at 8.4 GHz (see Figure 2.2) the configuration of the shell can still be seen although the bright feature B is barely detectable indicating that the radio spectrum was steepening at that region. This Parkes polarization **E**-vectors shown in Figure 2.2 confirmed the high degree polarization that was earlier found at 2.7 and 5 GHz (Dickel & Milne, 1976; Milne & Dickel, 1974a, 1975; Milne & Dickel, 1974b).

The total MOST CLEANed flux density was 7 Jy while for Parkes was deduced to 9 Jy. In the field of view of MOST at 843 MHz and Parkes at 8.4 GHz two possible planetary nebulars had been identified and marked in both Figure 2.1 and 2.10. PN 7-3°1 with MOST at 843 MHz at 15 ± 5 mJy. Also, it was detected with Parkes at 8.4 GHz at 78 ± 10 mJy (Perek & Kohoutek, 1967). PN 7-3°2 was not detected at 843 MHz with MOST but was related to a 'hole' in the 843 MHz emission and its detection with Parkes at 8.4 GHz was very doubtful. From MOST observation, Milne et al. (1986), suggested a distance of 4.5 ± 1.5 kpc to G7.7-3.7 based on surface brightness - diameter relation, Σ-D.

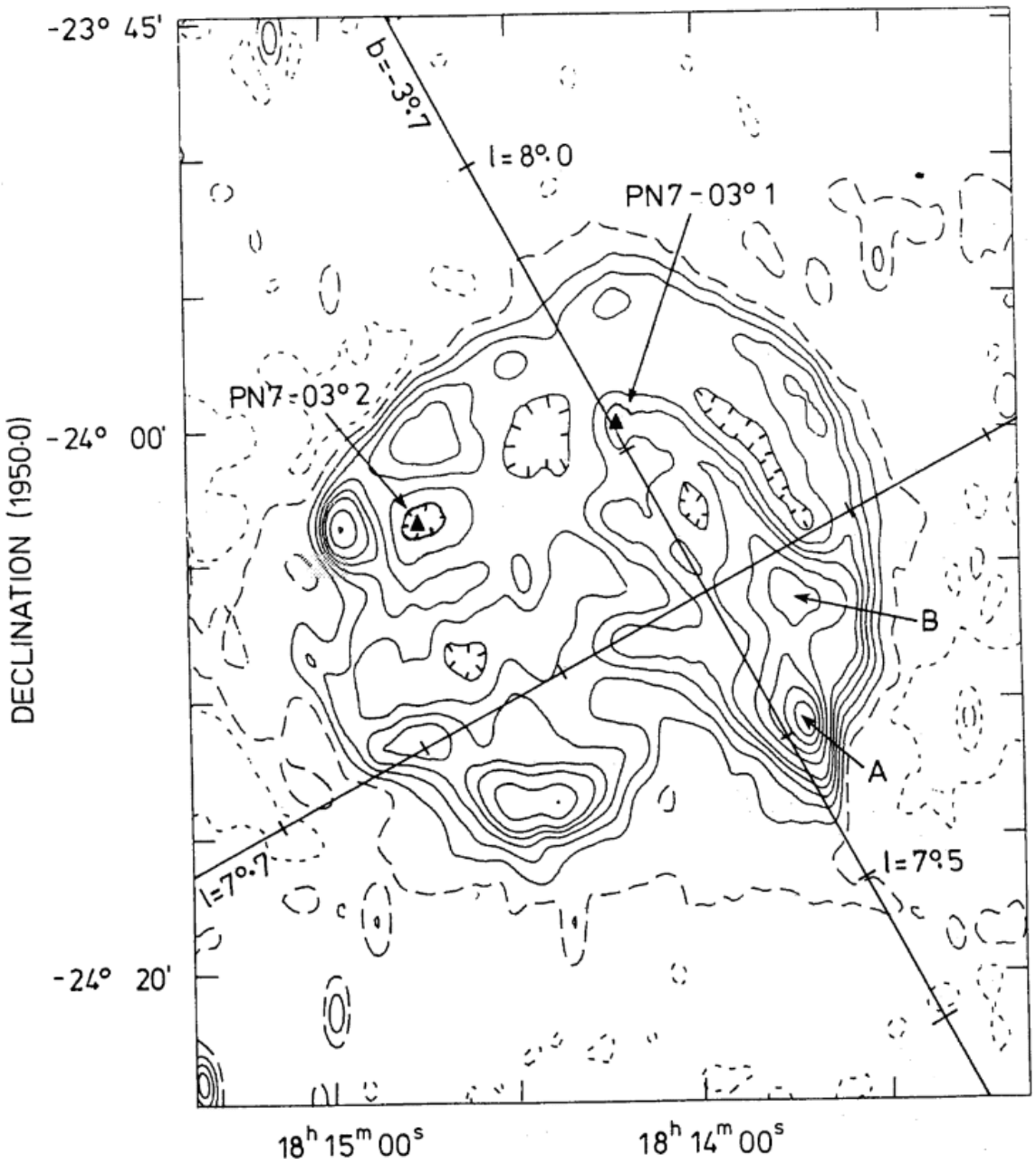

Figure 2.1: MOST intensity contours of the CLEANed radio map of G7.7-3.7 at 843 MHz. The levels of the contours are 0 and 10 (dashed), 20, 30, 40, 50, 60, 80, 100, 120 and 140 mJy/beam. Fringed contours shows the isolated minima. The beam size is 44″ EW × 108″ NS. The steep-spectrum regions are indicated by letters A and B. Also, the positions of the planetary nebula PN 7-03°1 and PN 7-03°2 are shown in this map. Source: see figure 1 in Milne et al. (1986).

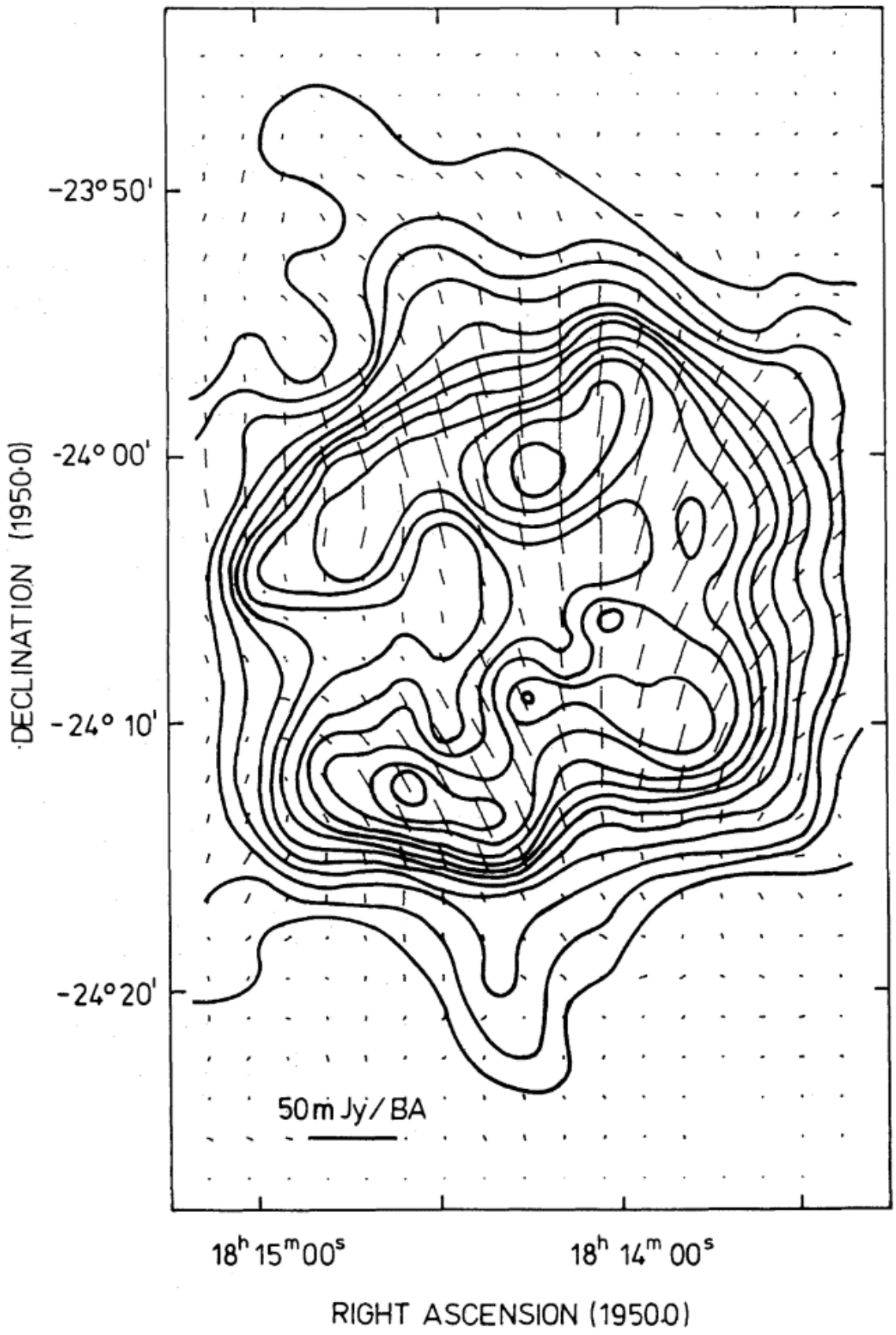

Figure 2.2: Total-power contours of G7.7-3.7 at 8.4 GHz and it's polarization **E**-vectors. The contour unit is 14.3 mJy/beam, and the half-power beamwidth is 3′. The scale of polarization intensity is indicated on the map. Source: see figure 2 in Milne et al. (1986).

A decade later, Dubner et al. (1996) observed G7.7-3.7 with VLA, as a faint extended source with an appearance of a nearly circular source with extended bright regions in the west and south boundaries with unresolved peak to the east border as in Figure 2.3. The interior of the remnant was filled with diffuse emission. The bright eastern spot appears to be connected with the maximum to the west by a non-thermal arc across the remnant. VLA resolves an angular size of 21.8′ ± 1.1, flux density of $S_{1.4GHz}$ = 9.9 ± 0.1 Jy and the surface brightness, Σ, at 1 GHz evaluated to $\Sigma_{1GHz} \simeq 3.5 \times 10^{-21}$ W m^{-2} Hz^{-1} sr^{-1}.

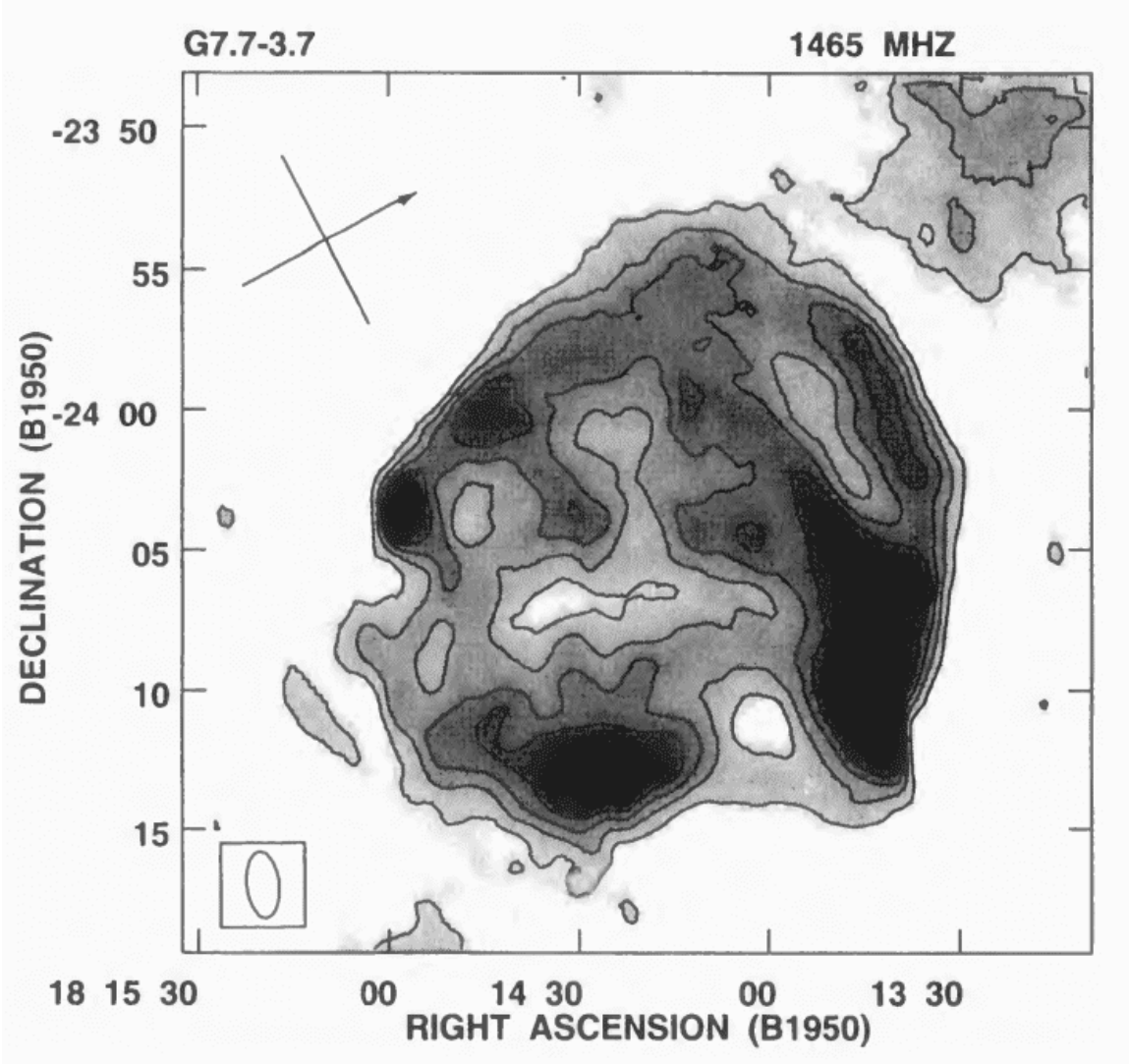

Figure 2.3: VLA + IAR continuum view of G7.7-3.7 at a frequency of 1465 MHz. The image was obtained using a beam size of 71″ × 35″. The grey scale depicts a range of flux values spanning from 8 - 45 mJy/beam. Contour lines are overlaid on the image at specific levels, including 10, 15, 20, 25, 30, 35, 40, 50, 60, 70, 80, 90, and 100 mJy/beam. Additionally, a large cross is present in the image, indicating the orientation of galactic coordinates, with the arrow pointing towards the galactic plane. Source: see Figure 1 in Dubner et al. (1996).

The most recent full stokes MeerKAT *L*-band (856 - 1712 MHz) observation of G7.7-3.7 at 1335 MHz by Cotton et al. (2024b) at a resolution of 10″ (see Figure 2.4) resolves it's shells into very many thin filaments with a very faint blowout or ear in the south-eastern area. The blowouts indicated that something was breaking through the outer edges of G7.7-3.7, most likely the weakening of the magnetic field at those outer edges. The flux density, S, was $S_{1335MHz}$ = 5.2 ± 0.4 Jy and an angular diameter of ∼27′ which show missing large-scale emission, filtered by the interferometer.

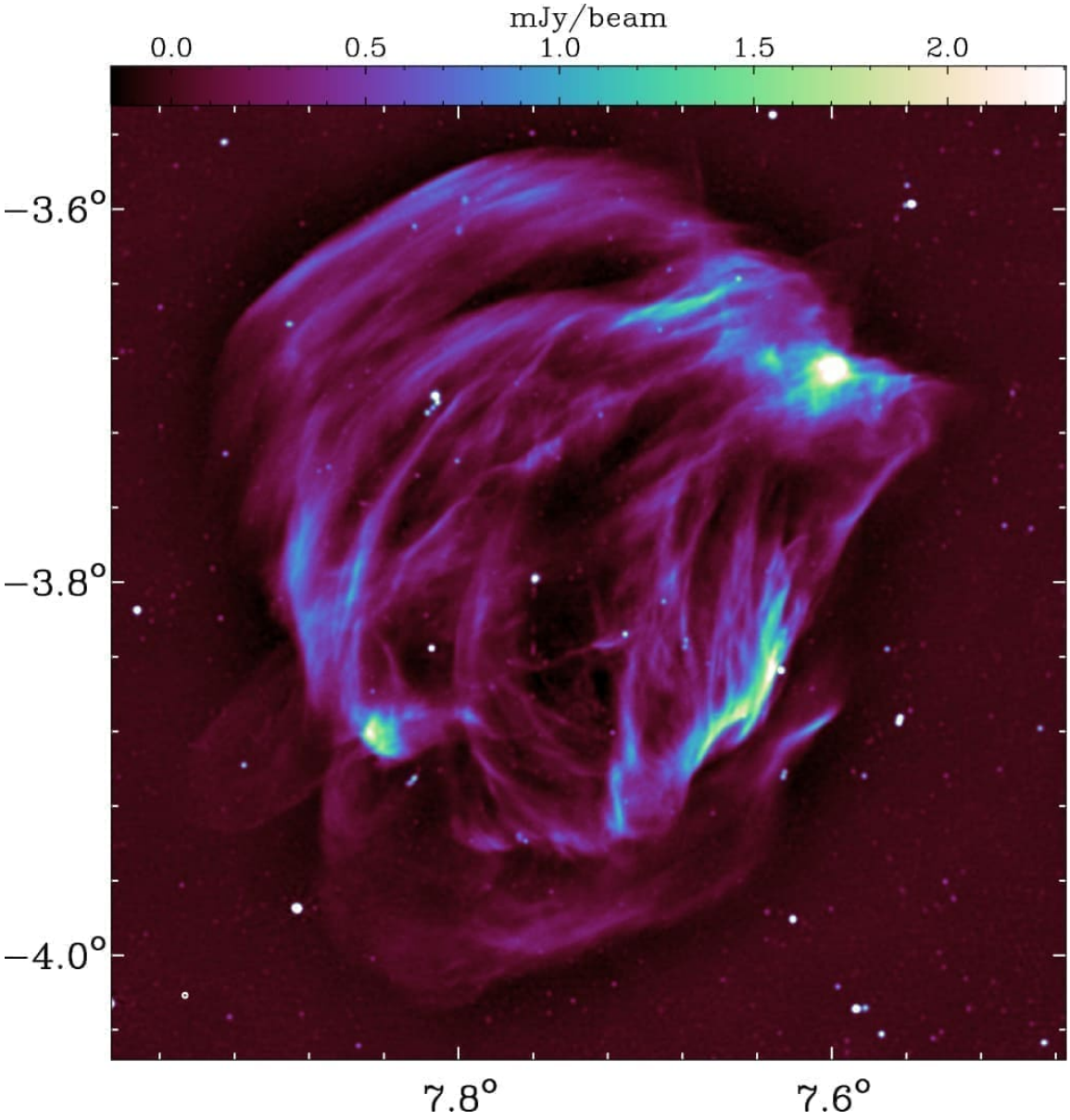

Figure 2.4: The Total power MeerKAT image of G7.7-3.7 at 1335 MHz in the resolution of 10″. Source: see figure 7 in Cotton et al. (2024b).

2.3.1 Spectral Index Distribution of G7.7-3.7

Milne et al. (1986) inspected the spectral index, α, (S = ν^{α}), between 843 MHz (MOST) and 8.4 GHz (Parkes) and generated spectral index distribution throughout G7.7-3.7 as in Figure 2.5. The average spectral index was α = -0.32 ± 0.05 which was a fairly flat spectrum. In Figure 2.5, steeper spectral index, α ∼-0.6, was observed in the south-western side of G7.7-3.7 with bright features (A and B in Figure 2.1). In the VLA observation, Dubner et al. (1996), the spectral index was evaluated to $\alpha \simeq$ -0.32 and concluded that G7.7-3.7 has a flat and uniform spectrum. In addition, the steep spectrum (α ∼-0.6) region in a bright spot in the western observed by Milne et al. (1986) was also identified in VLA observation. This steeper spectral index (α ∼-0.6) region than the rest part of the remnant was a common feature of an extragalactic object. Thus Milne et al. (1986) suggested this bright feature to be a chance of superposition of an extragalactic double source. However, from the VLA observation Dubner et al. (1996) proposed that this high emissivity region could be a knot of brighter emission.

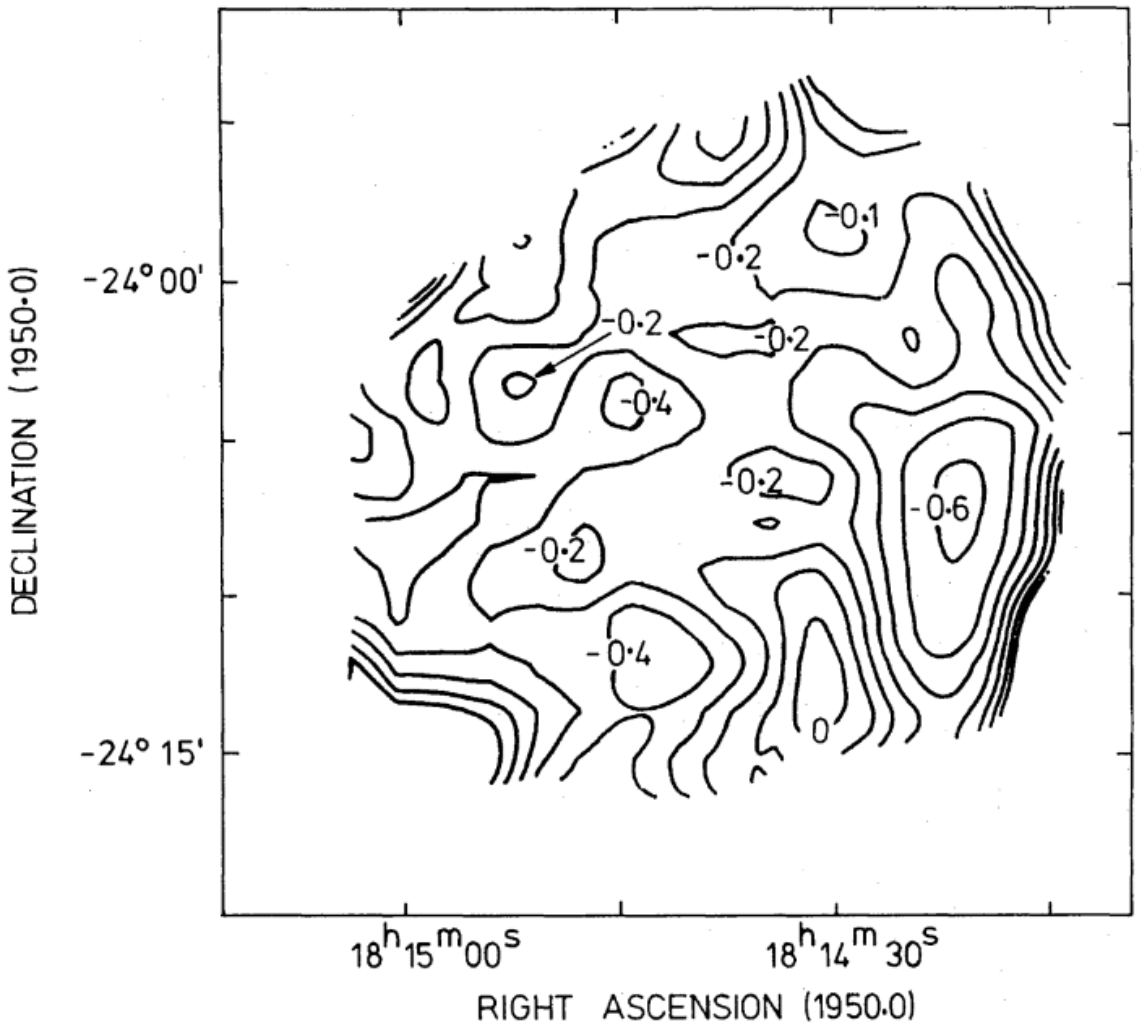

Figure 2.5: The spectral index distribution between 843 MHz and 8.4 GHz for G7.7-3.7 at a resolution of 3′. The contours shown are for total power levels greater than 10 % of the relevant peak value at either frequency. Source: see figure 3 in Milne et al. (1986).

2.3.2 Polarization Study of G7.7-3.7

Comprehensive polarization studies of G7.7-3.7 were sparked by Milne et al. (1986) by comparing Parkes observations at 8.4 GHz and previous one at 5 GHz (Dickel & Milne, 1976; Milne & Dickel, 1974a, 1975). The magnetic field distribution at a resolution of 4.6′ overlaid on the MOST contour map at 843 MHz (see Figure 2.6) was quite smooth and neither tangential nor radial. VLA observation revealed G7.7-3.7 with a mean linearly polarized intensity at 1465 MHz with ∼10% of the total intensity. The western half of G7.7-3.7 and the interior filament that connects the eastern and western parts were filled

with polarized radiation as in Figure 2.7 although the orientation of the position angles of the electric vectors was not clear. However, in MeerKAT observation at 1335 MHz (see Figure 2.8) the strong filamentary structure showed significant polarization of G7.7-3.7. The *B* vectors, giving the projected orientation of the magnetic field of G7.7-3.7, are aligned with the filaments.

Milne et al., 1986 accessed the 8.4/5.0 GHz depolarization ratio and was fairly uniform with values between 1 to 2. However, higher depolarization ratios beyond 2 and up to 5 were localized near the bright feature which has a steep spectrum in the south-west of G7.7-3.7. Finally, Faraday's rotation had moderate values over most parts of G7.7-3.7, falling between +100 to +200 radm^{-2} but higher values beyond this up to about +1100 radm^{-2} in a small region in the south-west bright spot. Cotton et al., 2024b, found that Faraday rotation of G7.7-3.7 had a steep gradient with the largest gradients in the north-west as depicted in Figure 2.8.

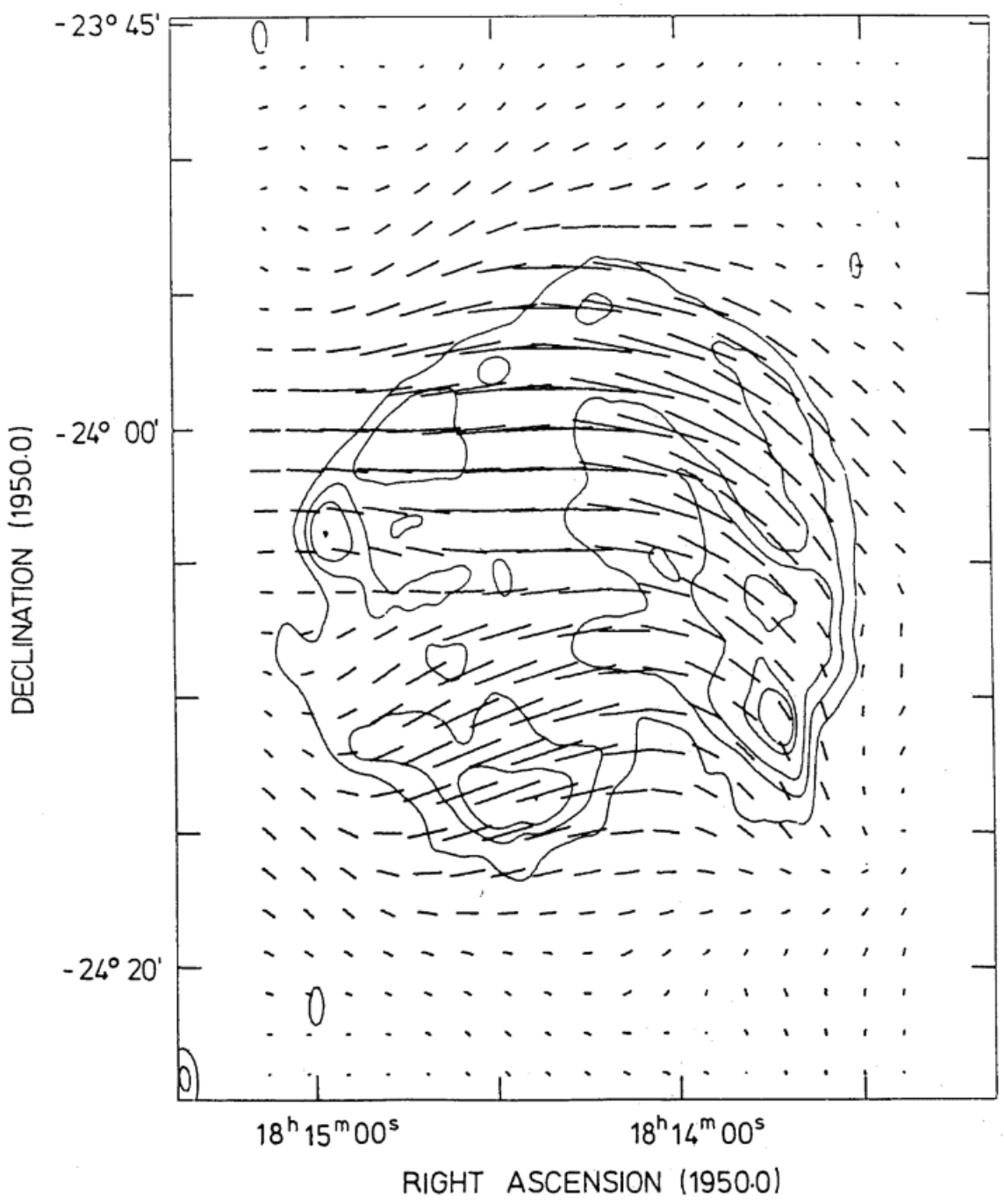

Figure 2.6: The direction of magnetic field of G7.7-3.7 at a resolution of 4.6′ superimposed on selected contours from the higher-resolution 843 MHz MOST map (see Figure2.1). Source: see figure 6 in Milne et al. (1986).

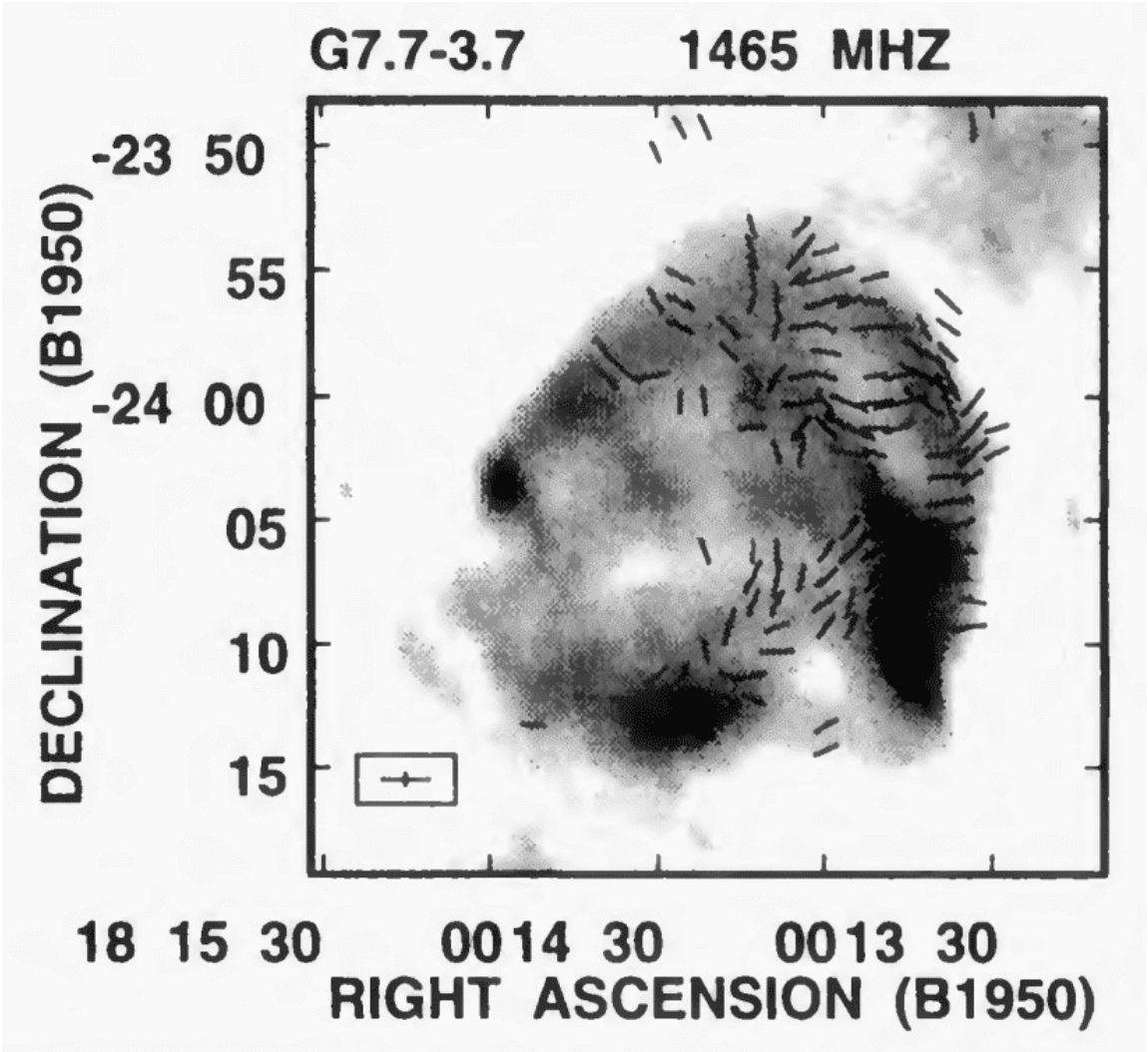

Figure 2.7: VLA linear polarization distribution of G7.7-3.7 at 1465 MHz overlaid on a grayscale depiction of the total intensity at the same frequency. The orientation of the vectors indicates the electric field's direction. Source: see figure 2 in Dubner et al. (1996).

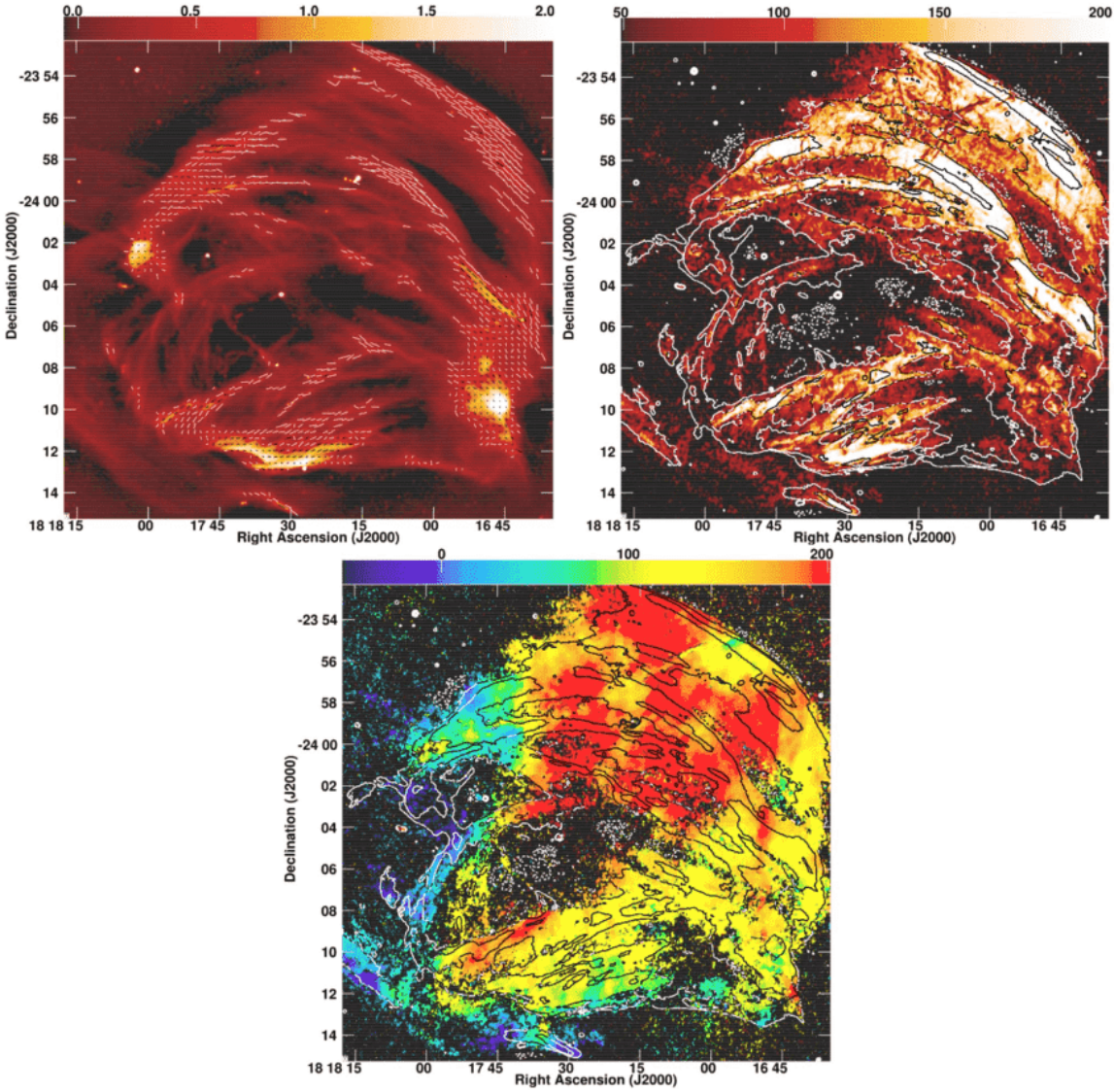

Figure 2.8: G7.7-3.7 MeerKAT Polarimetry. Top left: bias-corrected fractional polarization B vectors on heat image of Stokes I; scale bar labeled in mJy/beam at top. Top right: bias-corrected polarized intensity as heat image with scale bar labeled in μJy/beam on top; Stokes I contours at -0.1, 0.1, 0.4, 1.6, 6.4, and 25.6 mJy/beam. Bottom: peak Faraday depth in color given by scale bar at the top with Stokes I contours as shown in the top right. Source: see figure 57 in Cotton et al. (2024b).

2.4 X-ray Morphology of G7.7-3.7

X-ray morphology of G7.7-3.7 by Zhou et al., 2018 as shown in Figure 2.9 revealed an arc-like feature in the south. There was a disparity between X-ray brightness and radio brightness in the arc center where X-ray emission was fainter while radio emission was brightest. Apart from the southern arc which was the only bright X-ray feature, very diffuse and dim X-ray emission was detected inside the eastern radio feature.

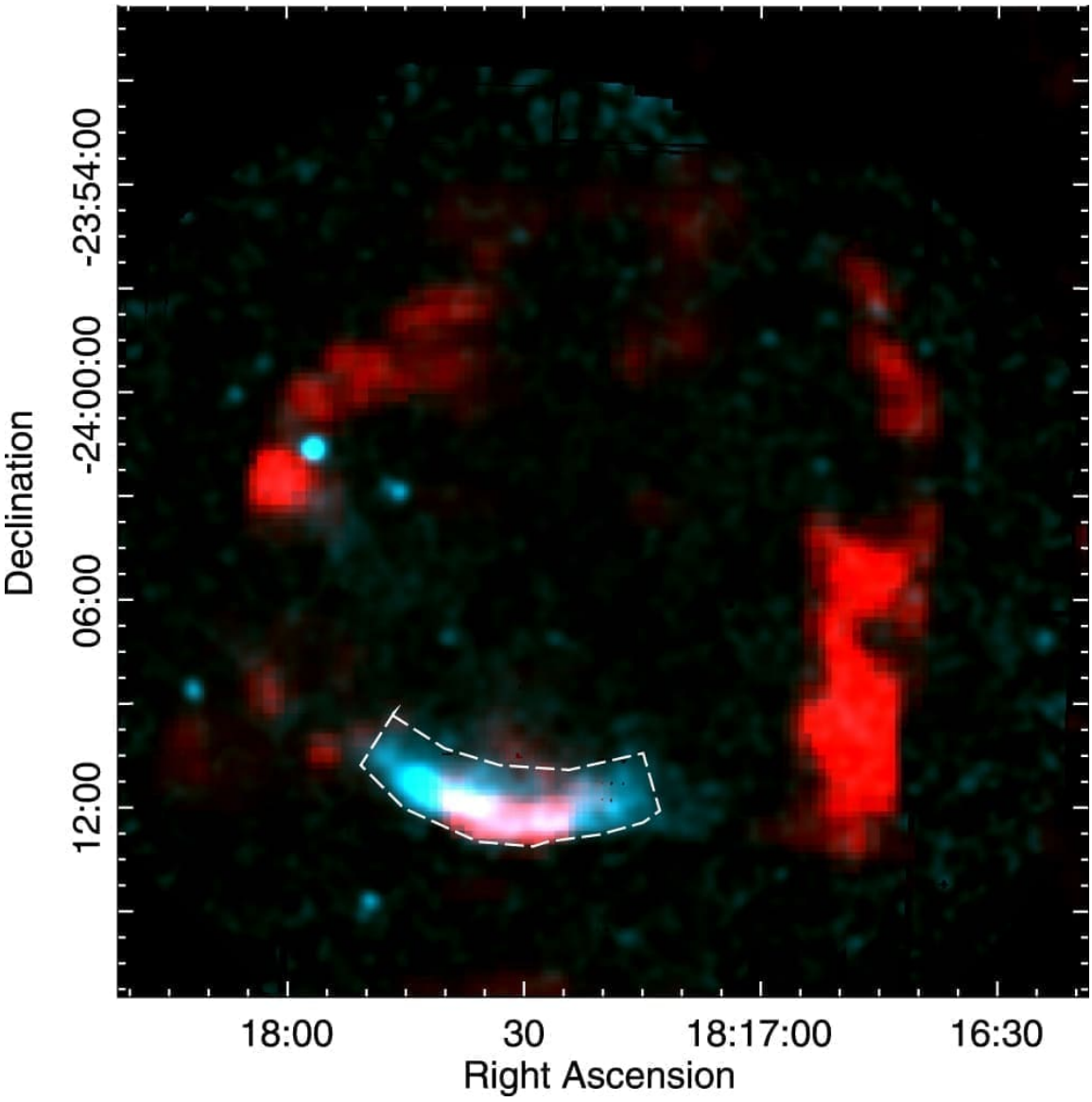

Figure 2.9: A composite picture of G7.7-3.7 that combines X-ray data in cyan and radio data at 1.4 GHz in red. The X-ray image was crafted from observations collected by the *XMM-Newton* observatory's pn and MOS instruments in 2012, specifically using OBSID: 0671170101. This X-ray image underwent vignetting correction, instrumental background subtraction, and adaptive smoothing to achieve a signal-to-noise ratio of 10. Source: see figure 1 in Zhou et al. (2018).

The region surrounding the southern arc was extracted by Zhou et al. (2018), for spectroscopic analysis to study the X-ray arc of G7.7-3.7. The X-ray photons detected mostly have an energy of <2 keV. At 1.33 keV, a He-like Mg line was detected and at ~1.85 keV, a He-like Si bump indicating that the emission had a thermal origin. The spectroscopic analysis showed that G7.7-3.7 was not much absorbed from its low foreground absorption N_H = 3.5 ± 0.5 × 10^{21} cm^{-2} indicating that the SNe was visible with the naked eye.

The G7.7-3.7 spectra were characterized by a thermal component that was not fully ionized with an electron temperature $kT = 0.5^{+0.3}_{-0.1}$ keV and with subsolar abundances. The low abundances indicated that the X-ray emission originated from shocked ISM instead of from the ejecta. The under-ionized plasma density, n_H, was estimated to be $n_H = 0.53^{+0.18}_{-0.15}$ cm^{-3} using best-fit X-ray volume emission measure. G7.7-3.7 age was inferred from the ionization timescale, τ, as its plasma was under-ionized using $\tau = n_e t$ where n_e is the electron density and t is the time elapsed as the gas is shock heated. Thus, the G7.7-3.7 shock age was estimated to be t = 1.2 ± 0.6 kyr from the low ionization timescale, $\tau = 2.4^{+1.1}_{-1.3} \times 10^{10}$ cm^{-3} s obtained from spectra results and the best-fit H density. This small shock age indicated that G7.7-3.7 was a young SN whose SNe could have been possibly observed by ancient astronomers.

The consistent age and position of G7.7-3.7 with guest star 386, which was visible with the naked eye for 2-4 months, suggested that the latter was an SNe that resulted in G7.7-3.7. The association of G7.7-3.7 with guest star 386 suggested that the SNe was a low-luminosity SNe, probably a low-luminosity Type IIP, explaining the small visibility of 2-4 months of the guest star. Zhou et al. (2018) suggested that G7.7-3.7 was likely expanding into a low density ($\leq$0.1 cm^{-3}) environment, explaining the X-ray brightness being low. There is a likelihood of ambient density being non-uniform as indicated by non-spherical radio morphology and intense X-ray emission in the south.

2.5 Optical Morphology of G7.7-3.7

In optical emission studies of G7.7-3.7, Domček et al. (2023) detected two faint filamentary structures, named A and B in Figure 2.11, in Hα + [NII], [OIII] and narrowly in [SII] narrow-band images only. These filaments are elongated in the east-west direction and located in the southern part of G7.7-3.7 in a region outlined by a dashed rectangle in Figure

2.10. These optical filaments were similar to those detected by Parker et al. (2005) in the SuperCOSMOS Hα imaging survey. Filament A was emitting mainly in Hα + [NII] and marginally in [OIII] (see Figure 2.11) and located in front of the intense X-ray. Filament B was emitting in Hα + [NII] and [OIII] with a very faint optical emitting structure in [SII] (see Figure 2.11) and lies in the fainter X-ray position. Filament B as compared with Filament A has a more diffuse optical emitting structure. In the Hβ image there was no significant structure even in 2-hour exposure time.

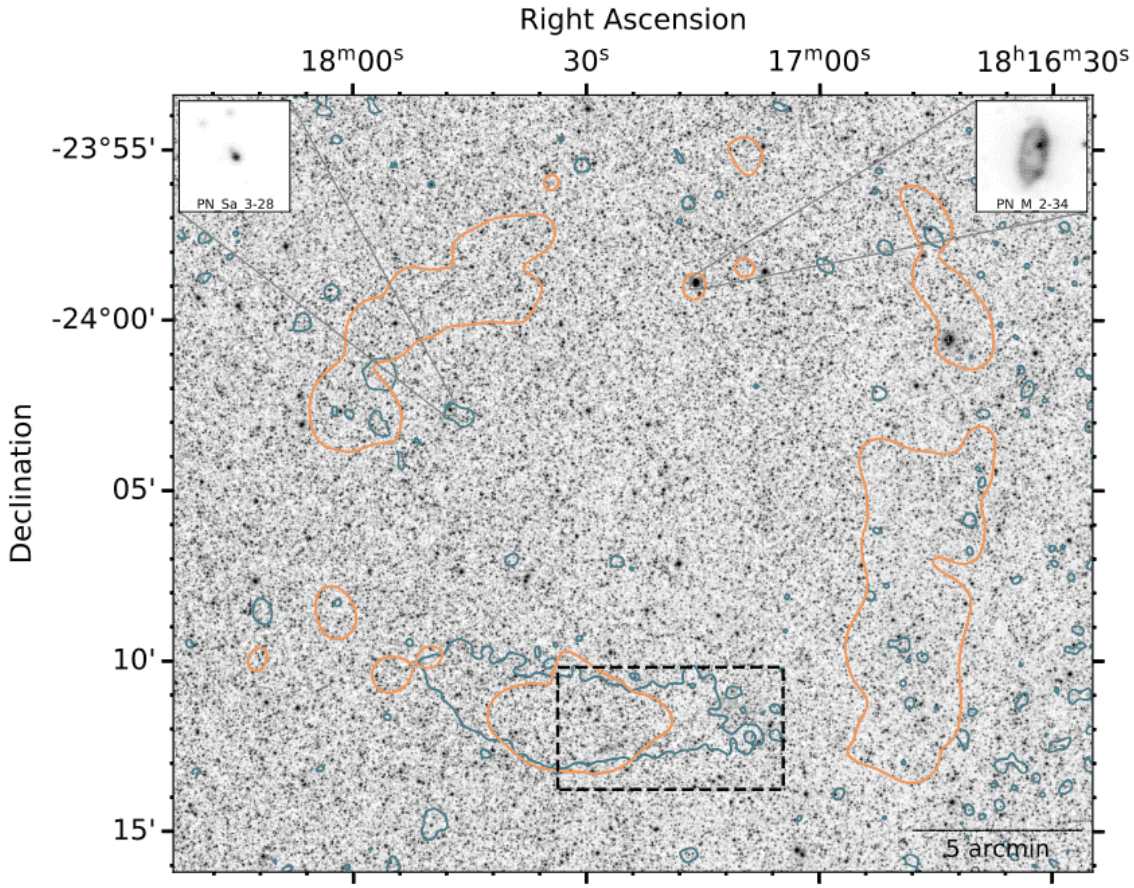

Figure 2.10: A composite Hα + [NII] count rate image of G7.7-3.7. In this representation, regions outlined in orange depict the 1.4 GHz NVSS radio contours at a flux level of 0.003 Jy/beam, (Kaplan et al., 1998), while regions in blue represent *XMM–Newton* X-rays in the (0.5-5.0) keV range with contours set at a flux level of 7×10^{-5} ct s^{-1} (for a comprehensive view of both radio and X-ray data (see Figure 2.9) (Zhou et al., 2018)). Within this image, a dashed rectangle outlines a region where optical emissions were detected and subsequently analyzed as in figure 2.11. The field-of-view also encompasses two planetary nebulae (PN Sa 3-28 (or PN 7-03°2), (Milne et al., 1986; Perek & Kohoutek, 1967), and PN M 2-34 (or PN 7-03°1), (Milne et al., 1986), visible in the upper corners of the figure, with differing scaling and magnification enhanced by a factor of 10. Source: see figure 1 in Domček et al. (2023).

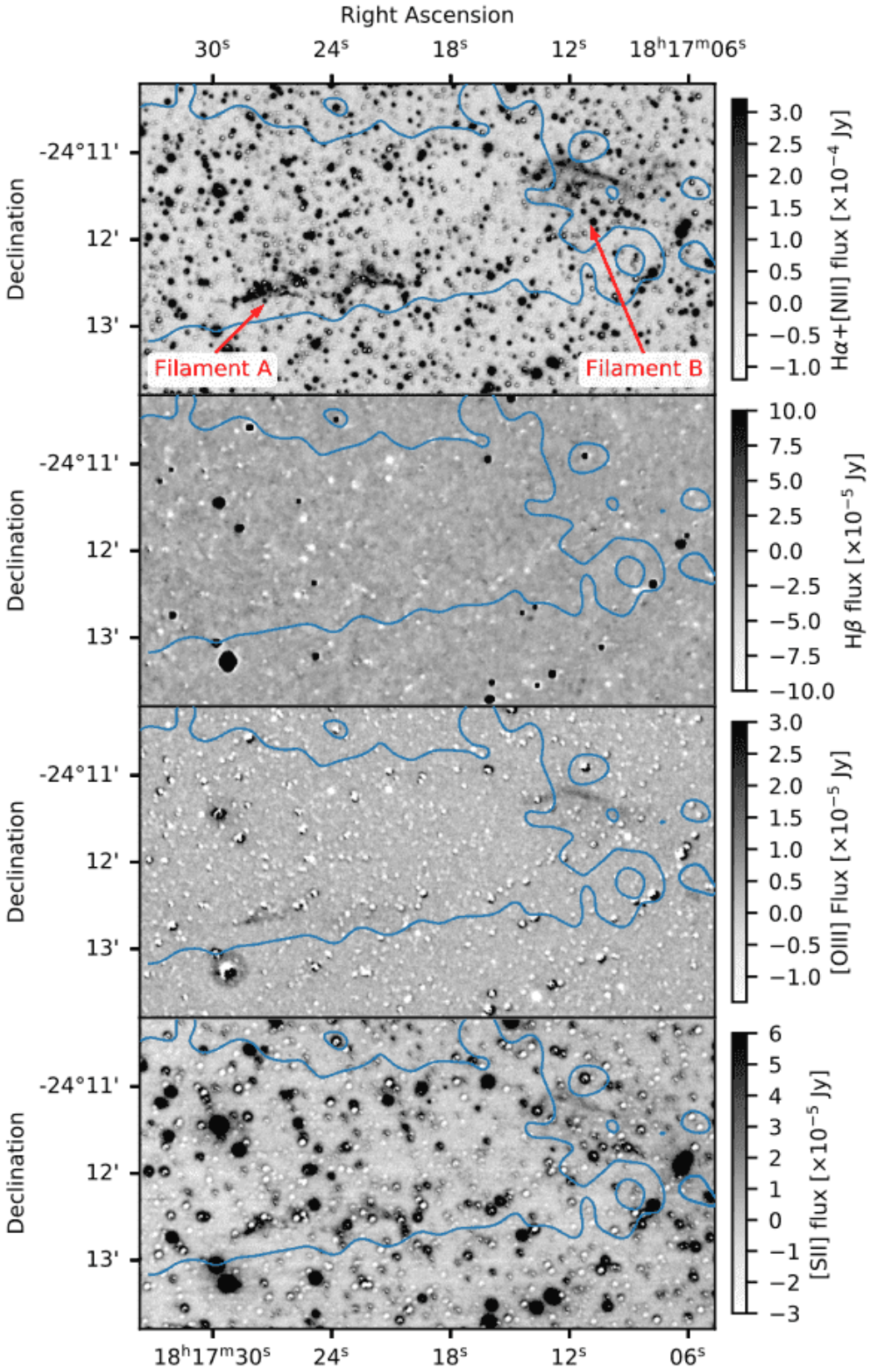

Figure 2.11: Images of G7.7-3.7 with continuum subtracted, observed through narrow-band filters showing Filament A and B, are presented from top to bottom. These filters include Hα + [NII], Hβ, [OIII], and [SII]. Source: see figure 2 in Domček et al. (2023).

The low-resolution long-slit spectroscopy of Filament B was obtained to determine the nature of optical emission in G7.7-3.7. The spectroscopic analysis of Filament B didn't show any [OIII] line emission despite being detected in the [OIII] image in Figure 2.11. However, the missing [OIII] emission lines in Filament B were explained by the slit position. The spatial offset of $\sim 2''$ was found between Hα + [NII] and [OIII] images of Filament B. This offset between Hα and [OIII] is expected in SNRs and shocked gases in general (Boumis et al., 2022). The gas which is just behind the shock is highly ionized and optical emission lines like [OIII] are detected (Domček et al., 2023). After the gas cools down and recombines, it results further in Hα optical emission back from the shock front. Thus, the spatial offset is consistent with the filament moving away from the geometric center of G7.7-3.7.

The [SII]/Hα line ratio diagnostic of Filament B revealed a large ratio, [SII]/Hα = (1.6-2.5), which is expected for shock-related SNRs. Based on the spectroscopic observed [SII] doublet ratios in two regions of Filament B, the n_e upper limit of the gas of both regions falls $n_e < 400$ cm^{-3} and $n_e = 600$ cm^{-3} in the respective regions. These small n_es are consistent with evolved SNRs (Domček et al., 2023). The large emission ratios of [NII]/Hα of regions along Filament B, [NII]/Hα > 2 (see table 3 in Domček et al. (2023)), were observed from the spectroscopic data. This suggested that the gas was enriched in nitrogen. The enrichment of nitrogen in the shocked gas showed the existence of circumstellar materials near the southern shell of G7.7-3.7. Also, the shell gas can be a mixture of ISM and circumstellar materials. Regarding the optical formation mechanism of G7.7-3.7 filaments, Domček et al. (2023), concluded that it resulted from the collision of G7.7-3.7 blast with a dense circumstellar shell lying close to the southern boundary.

The collective findings from these studies showcase the multi-faceted nature of G7.7-3.7

and its interactions across various spectral domains. These findings also illuminate the multi-faceted nature of G7.7-3.7 and hint at potential interactions with its environment that warrant further exploration. While they have each contributed valuable insights, the lack of a unified, multi-wavelength investigation has left key questions regarding the remnant's evolution, precise age, distance, and its interaction with the ISM unanswered. This gap in knowledge underscores the necessity of a comprehensive multi-wavelength study that brings together these different lines of inquiry. The use of advanced radio astronomy techniques, particularly MeerKAT, presents an opportunity to integrate these disparate observations into a holistic understanding of G7.7-3.7, thereby elucidating its astrophysical properties and historical significance.

CHAPTER THREE: METHODOLOGY

3.1 MeerKAT Telescope

MeerKAT is a prominent radio telescope located in the Karoo region of South Africa. It is a significant milestone in the field of radio astronomy and is part of the larger Square Kilometre Array (SKA) project, which aims to build the world's largest and most sensitive radio telescope (Jarvis, 2012). MeerKAT has its roots in the Hartebeesthoek Radio Astronomy Observatory, where early work was initiated in the 1990s (Booth et al., 2009; Booth & Jonas, 2012). The project received substantial support from the South African government and was officially launched in 2007 (Booth & Jonas, 2012).

MeerKAT boasts an array of 64 radio antennas that are positioned across the arid landscape of the Karoo region of South Africa (Booth et al., 2012; Jonas & MeerKAT Team, 2016). These dishes are closely packed within an area spanning 8 Km, with 48 dishes in a 1 km radius while the remaining 16 dishes in 8 km outward, giving MeerKAT its distinctive and eye-catching configuration (Chibueze et al., 2022; Jonas & MeerKAT Team, 2016). With this configuration, the MeerKAT array's shortest and longest baselines are 29 m and 8 km, respectively, offering angular scales from 5 arcseconds to 27 arcminutes at 1283 MHz, the central frequency of the L-band receiver (Chibueze et al., 2022; Jonas & MeerKAT Team, 2016). Each antenna is equipped with a 13.5-meter diameter dish, which, when combined, creates a highly sensitive and powerful radio telescope (Jonas & MeerKAT Team, 2016). These antennas are designed to observe radio frequencies ranging from 580 MHz to 14.4 GHz, making MeerKAT suitable for a wide range of astronomical studies (Jarvis, 2012).

MeerKAT telescope is designed to conduct radio holographic measurements across its sup-

ported observing bands, 544−1087 MHz (UHF band), 856−1711 MHz (L band), 1750−3499 MHz (S-band) and 8-14.4 GHz (X band) offering a wide range of radio frequency coverage from 544 MHz to 14.4 GHz (de Villiers, 2023; Jarvis, 2012). One of the most impressive features of MeerKAT is its exceptional sensitivity and imaging capabilities. The telescope's advanced technology allows for high-resolution and high-quality observations of the radio universe, enabling astronomers to peer into the cosmos with unprecedented detail. MeerKAT is a precursor to the SKA project and has already made significant contributions to our understanding of the radio sky. It is a testament to the South African commitment to advancing radio astronomy and a beacon of cutting-edge technology in the field.

3.2 MeerKAT Observation of G7.7-3.7

G7.7-3.7 was observed with 62 antennas of the MeerKAT array on 20 January 2023 (proposal ID: SCI-20220822-CV-01[1]) at the L-band (856 MHz to 1712 MHz) with a bandwidth of 856 MHz (Camilo, 2018; Jonas & MeerKAT Team, 2016; Jonas, 2009; Mauch et al., 2020). The observation comprises four fields: J1939-6342 (primary calibrator), J1331+3030 (polarimetric calibrator), J1833-2103 (secondary calibrator) and FRB20220330 (target source). All 11 scans were carried out with a total track time of 9284 s (~2.58 hours) and a mean integration time of ~8 s. The primary calibrator, J1939-6342, was used for bandpass and flux calibration, positioned 0.0384″ from the nominal position. FRB20220330 was the primary target with J1833-2103 as the secondary calibrator for phase and amplitude calibration located 4.935° apart. During the observation; J1939-6342 was scanned for 600 s (10 min), J1331+3030 for 584 s (~9.73 min) and J1833-2103 for every 104 s (~1.73 min) after 1783-s (~29.72-min) scan of FRB20220330. SKARAB cor-

[1]https://archive.sarao.ac.za/.

relator was used for data correlation with a bandwidth of 856 MHz and 4096 channels of ~0.209 MHz/channel and a central frequency of 1284 MHz (Camilo, 2018; Hickish et al., 2016).

3.3 MeerKAT Data Reduction

The OXKAT pipeline[2], semi-automated MeerKAT data analysis pipeline, was used to reduce the data (Heywood, 2020). OXKAT utilizes a collection of radio interferometry data flagging, calibration and imaging publicly available software packages. During flagging, the known radio frequency interference channels are normally flagged out. Autoflag using tricolour for target fields was executed to flag other possible radio frequency interference. OXKAT pipeline employs CASA custom tasks for cross-calibration (McMullin et al., 2007). WSClean imager with weight briggs of -0.3, multi-scale and wide-band deconvolution algorithms enabled were used to deconvolve and image the target data and diffuse emission present in the target fields (Offringa et al., 2014).

3.3.1 OXKAT General Workflow

The OXKAT general workflow is broken down into stages described as follows:

I. **Setups**: These are Python scripts that create bash files containing sequential calls to radio astronomy packages or other OXKAT Python scrips. Sequential processing jobs are broken down into stages GET_INFO, 1GC, FLAG, 2GC, 3GC_peel and 3GC_facet. It is crucial to examine the state of the processing before continuing to the preceding stage. However, 3GC peeling and facet-based calibration stages are optional and require the user to provide some region files to guide the direction-dependent calibration. The MeerKAT data, to be processed, must be in a Measure-

[2]https://github.com/IanHeywood/oxkat.

ment Set (MS) containing target scan, and primary and secondary calibrator scans. The content of the root OXKAT repo is cloned into an empty folder. Placing symlink to (or copying) MS in the same folder sets everything to start running the following setup scripts sequentially.

II. **GET_INFO**: This initial setup script determines the observing band (UHF, L-band or S-band), examines the MS contents to identify target and calibrator fields, pair targets with the secondary calibrator and selects a reference antenna based on minimal flag percentages. Three log files are produced: msinfo log file containing observation information, sun log file listing the absolute and relative positions of the sun and moon on a per-scan basis and scantimes log files containing detailed information about the timestamps of each scan. Finally, writes relevant information to a JSON file that is read and relied upon by subsequent scripts.

III. **1GC**:In this stage, CASA is mostly used to execute the provided processing scripts. The 1GC.py setup scripts look for a single MS in the working folder and perform the following tasks: duplicate the source MS, averaging it to 1024 channels, rephase the visibilities of the primary calibrator to correct for position errors, execute basic flagging commands to all fields, run autoflaggers on the calibrator fields, derive and apply delay (K), bandpass (B), gain (G) calibrations from the primary and secondary calibrators to all calibrators and targets, plot the gain tables and visibilities of the corrected calibrator data using ragavi-gains and shadeMS respectively and finally, split out the target data into individual MSs with the reference-calibrated data in the DATA column of the MS.

IV. **FLAG**: The FLAG.py script picks up where 1GC.py stops and executes the following

tasks for every target in the MS source: autoflag the target data, image the targets and generate a FITSmask of the field using tricolour, wsclean and local RMS thresholding respectively. The generated images will be available for examination in IMAGES folder generated automatically.

V. **2GC**: This 2GC.py script executes direction-independent self-calibration after FLAG.py for every target MS extracted from the source MS in the following steps: DATA column masked deconvolution using wsclean and FITS mask produced by FLAG.py, predict model visibilities using wsclean based on the resulting clean component model, self calibrate the data using CubiCal, CORRECTED_DATA masked deconvolution using wsclean, predict model visibilities from the CORRECTED_DATA image based on the refined model and refined the FITS mask based on the self-calibrated image and crop it if required by DDFacet.

VI. **3GC**: This is an optional script that performs direction-dependent self-calibration in two recipes in the form of 3GC_peel.py and 3GC_facet.py script. 3GC_peel.py used wsclean to model and CubiCal to peel a single, strong problem source from the visibilities and left a residual visibilities set to be imaged subsequently. 3GC_facet.py uses killMS to derive directional gain corrections that are used during imaging by DDFacet.

Deconvolution was done in 8 sub-band images centered from 0.909 GHz to 1.658 GHz of each 0.107 GHz wide band. The multiple-frequency synthesis (MFS) map was generated by WSClean, in joined-channel deconvolution mode with 1.284 GHz as the central frequency. Cubical software customary tasks were used in the OXKAT pipeline for self-calibration (Kenyon et al., 2018).

A circular synthesized beam of 5″.7 and a root-mean-square in the MFS image was 0.61 μJy/beam. The sub-band images have the central frequency of 0.909, 1.016, 1.123, 1.23, 1.337, 1.444, 1.551 and 1.658 GHz. Spectral index map (see Figure 4.2) was generated using CASA task immath after smoothing the resolutions of sub-band images to the resolution (8″.5 × 8″.5) of the 0.909 GHz sub-band image using CASA task imsmooth.

3.4 Retrieval of X-ray Data

We retrieved the most recent X-ray data (OBSID: 0840940101) from XMM-Newton Science Archive[3] (Zhou et al., 2018) for comparison with radio data. The XMM-Newton observation was conducted on 12 March 2020 using pn, MOS1 and MOS2 cameras all operating in full frame mode with a medium filter covering G7.7-3.7 whole. The total screened exposure time was 80 600 s (∼22.39 hours). The XMM-Newton data was reduced using the Science Analysis System software (SAS) and analyzed using XSPEC, AtomDB and SPEX as described in Zhou et al. (2018). The resulting structure for XMM-Newton X-ray emissions in G7.7-3.7 are shown in Figure 4.4

3.5 Retrieval of Optical Data

We also retrieved the recent optical data for G7.7-3.7[4] observed by 2.5 m Isaac Newton Telescope (INT) in La Palma Spain with Wide Field Camera (WFC) on August 22-25 2019 and June 23, 2022, Domček et al. (2023), to combine with X-ray and radio data. The field-of-view of ∼34′ × 34′ with 0.33″ pix^{-1} was set for the detector during observation. The narrow-band filters H α + [N II], H β, [O III], [S II], and H β were used to obtain the data while SDSS broad-band filters r′ and g′ were used for continuum subtraction. The narrow-band combined exposure times were 90, 15, 37 and 30 min respectively while for

[3]https://nxsa.esac.esa.int/.
[4]https://doi.org/10.5281/zenodo.5121367.

two broad-band filters was 5 min. The data reduction was done using THELI software as described in Domček et al. (2023). The generated optical data was archived in a Zenodo repository[5].

3.6 G7.7-3.7 Analysis Softwares

The research made use of the SAOIMAGE DS9 (Joye & Mandel, 2003), CASA (McMullin et al., 2007), PYTHON packages `APLpy` (Robitaille, 2019), ASTROPY (Astropy Collaboration et al., 2013), MATPLOTLIB (Hunter, 2007), and NUMPY (Harris et al., 2020). SAOIMAGE DS9 was used to visualize the reduced and retrieved G7.7-3.7 data. Python with packages such as `APLpy`, Astropy, MATPLOTLIB and NUMPY were used for the analysis of G7.7-3.7 data to generate visual images for MeerKAT radio data, X-ray data, optical data and the mosaic image by combining the three wavelengths data. It was also used to analyze and generate a visual image of the MeerKAT radio spectral index map. This MeerKAT radio spectral index map was generated using CASA immath task using sub-band images at 0.909 and 1.658 GHz.

[5]https://doi.org/10.5281/zenodo.5121367.

CHAPTER FOUR: RESULTS AND DISCUSSIONS

4.1 G7.7-3.7 Radio Image

The total power MeerKAT radio image of G7.7-3.7 (see Figure 4.1) with a circular beam of 5″.7 at 1284 MHz presents a fascinating structure with an average diameter of ~27′ centered at (18:17:24.8, -24:04:58.4). G7.7-3.7 has a strong bright blowout in the western boundary and extended bright filament in the southern perimeter with feather-like filaments seemingly disconnected from the western bright blowout. In the eastern, it has a faint blowout with a bright point source at the center. The north-west is occupied by very faint elongated filaments connecting the eastern point source and the western bright blowout. These filaments appear overlying on top of each other and moving progressively towards the north-west. This MeerKAT observation concurs with the previous radio observation of G7.7-3.7 (Cotton et al., 2024b; Dubner et al., 1996; Milne et al., 1986).

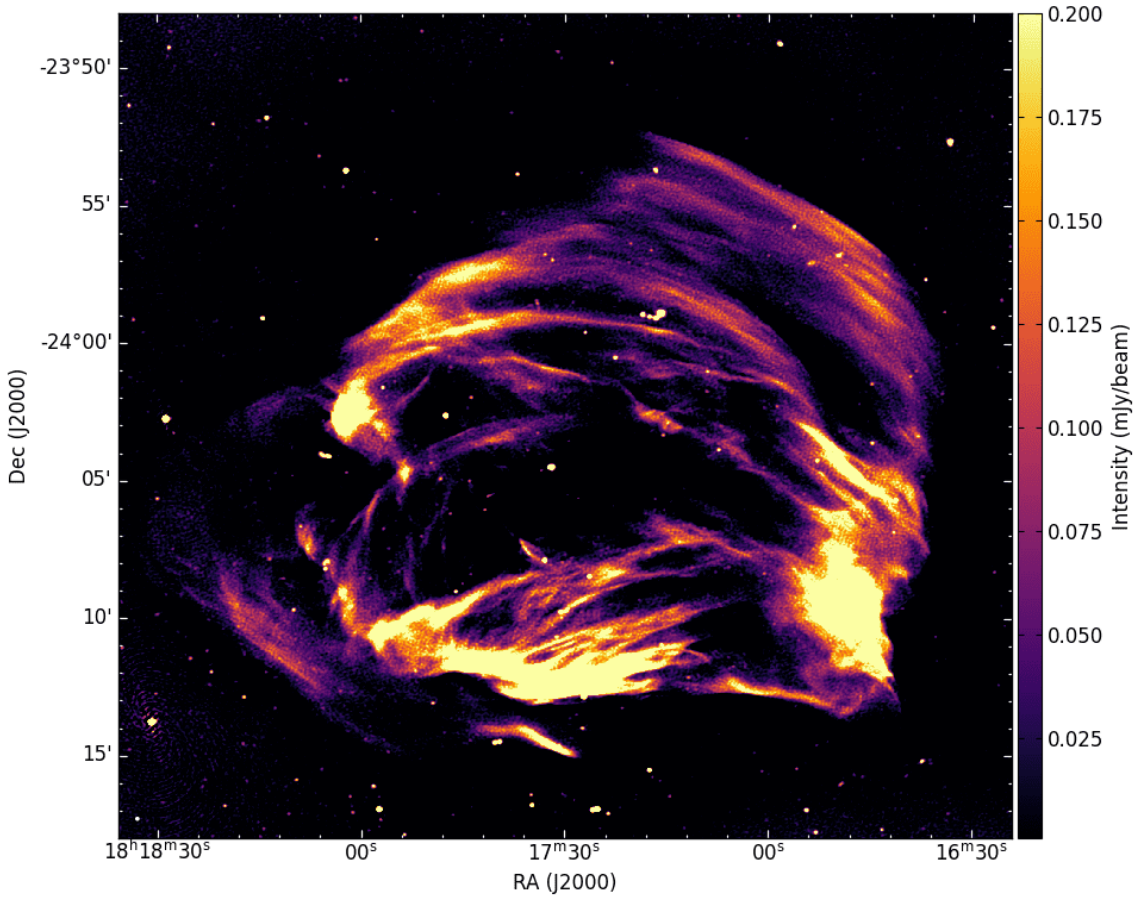

Figure 4.1: Total power MeerKAT radio image of G7.7-3.7 at 1284 MHz with a circular beam of 5″.7.

4.2 G7.7-3.7 Spectral Index Distribution

The spectral index distribution map of G7.7-3.7 (see Figure 4.2) reveals unique features with fluctuating spectrum, $\alpha \sim 0$ to -3, suggesting a strong synchrotron emissions with faint traces of thermal emissions for values towards $\alpha \sim 0$ (Ball et al., 2023; Martinez et al., 2023; Nayana et al., 2024). Specifically, the variation in spectral indices across different blowouts and filaments is particularly noteworthy. The brighter blowouts have less steep spectral indices ranging ~ -0.6 to ~ -1.2, while the dimmer and more diffuse filaments show very steep spectral indices, $\alpha \sim$ -3.

However, paying closer attention to the edges of the south blowout it is clear that there are spectral index values close to $\alpha \sim 0$ indicating that there are thermal emissions in the south.

The same observation is noted in the west and east blowouts, especially at the edges of those regions, although thermal emissions are not strong like synchrotron ones. These thermal emissions could result from the shock-heated gases from strongly shocked regions due to the collisions with the ISM.

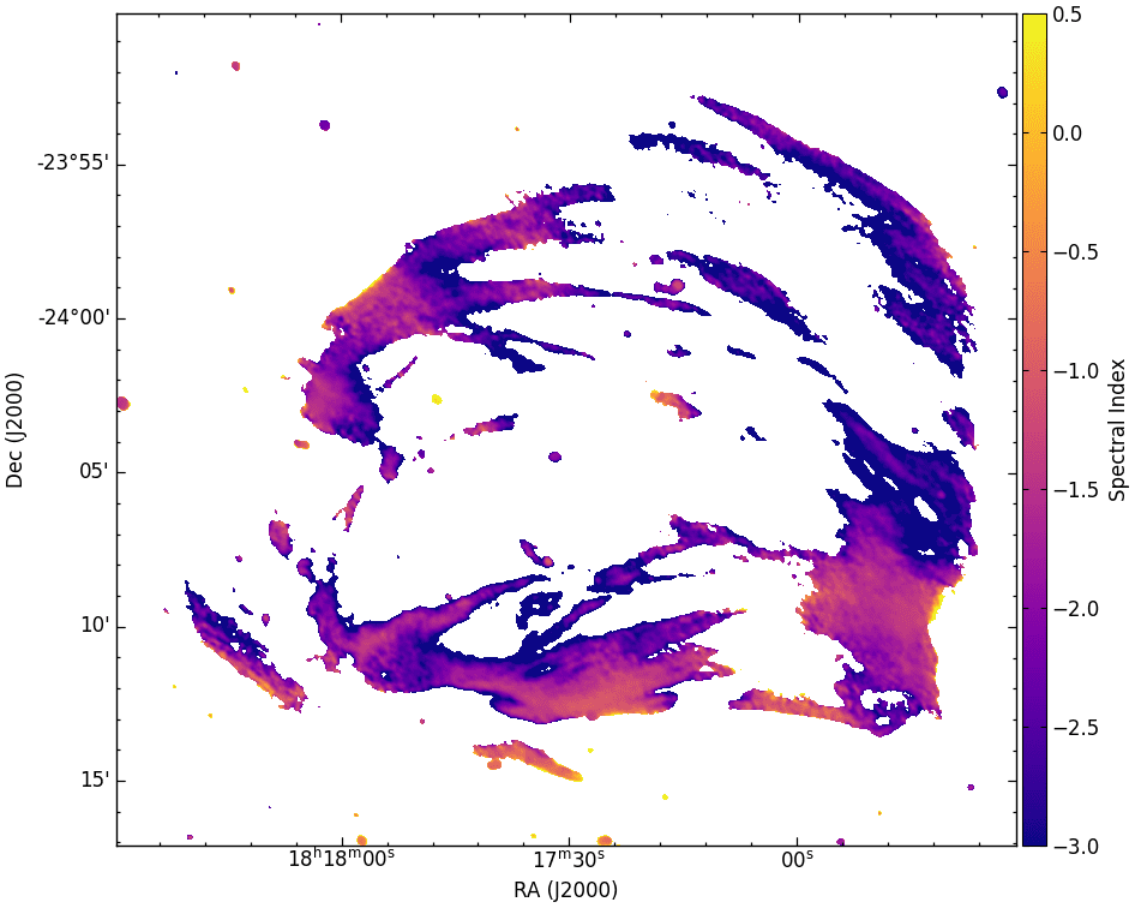

Figure 4.2: The distribution of spectral index of G7.7-3.7.

Generally, G7.7-3.7 has a fluctuating spectrum with strong synchrotron emissions and some traces of thermal emissions, which differs from previous studies by Dubner et al. (1996) and Milne et al. (1986) which reported a flatter and uniform spectrum with a steep spectrum, α = -0.6, in the western bright region. The variation in the spectral index observed within G7.7-3.7 can be attributed to a mechanism, reflecting the complex dynamics of G7.7-3.7. In the brighter radio blowouts, which are characterized by relatively less steep spectral indices ranging $\sim$ -0.6 to $\sim$ -1.2, shock acceleration processes may be at play, leading to the

acceleration of particles to higher energies to emit strong synchrotron emissions (Bresci et al., 2023; Huang et al., 2023; Kirk et al., 2023; Miceli, 2023; Nayana et al., 2024; Rajpurohit et al., 2024). As shocked electrons move back and forth across the shock front, they encounter irregularities and weakening of magnetic fields scattering them near the shock and gaining more energy (Rajpurohit et al., 2024).

On the other hand, in the dim and diffuse filaments with very steep spectral indices, $\sim$ -3, the observed steepening may be indicative of particles reaching the cut-off energy, Holman (2003), before reaching the higher energies or having low particle densities required to emit bright synchrotron radiation (Kumari & Pal, 2024). The diffuse emissions have a very steep spectrum which is consistent with the aging of the synchrotron spectrum owing to rapid energy losses resulting in faint emissions (Kumari & Pal, 2024; Rajpurohit et al., 2024; Shulevski et al., 2024). The very steep spectrum in faint emissions could be a consequence of turbulent re-acceleration of relativistic electrons dissipating energy rapidly and only very low energy radiations emitted (Benaglia, 2024; Kumari & Pal, 2024; Lovell et al., 2024; Riseley et al., 2024; Santra et al., 2024). Indeed, the spectral fluctuations may result from an inhomogeneous magnetic field and varying acceleration timescale of relativistic electrons (Riseley et al., 2024; Santra et al., 2024).

4.3 Origin of Bright Radio Emissions of G7.7-3.7

The emergence of three distinct bright radio emissions within G7.7-3.7 can be attributed to a multifaceted interplay of mechanisms, contributing to its localized enhancement of radio brightness. The resolved filamentary structure of G7.7-3.7 with blowouts along its western, southern, and eastern boundaries looks like its outer perimeter consists of mainly mass outflows (Cotton et al., 2024b). The non-uniform mass outflow of the progenitor star results in the non-uniform particle density distribution of the remnant. The shock front of

G7.7-3.7 accelerates many particles across it and traps them near it gaining high energies. This acceleration accumulates many particles in the shocked regions resulting in localized high densities of shocked particles in the west, south and east blowouts. The localized high densities of shocked particles of G7.7-3.7, result in localized knots of bright synchrotron radio emissions of G7.7-3.7.

However, the collision of the shock waves with ISM results in the formation of thermal emissions especially in the south blowout and at the edges of west and east blowouts. These traces of thermal emissions have been observed in the spectral index map (see Figure 4.2). The faint emissions along the filaments connecting the eastern and western blowouts with the spectral index of $\sim$ -3 comprises synchrotron emissions from aged particles that have dissipated a lot of energy due to turbulent re-acceleration. The variations in the magnetic fields within the remnant may contribute to the observed radio features (Chevalier & Fransson, 2006; Cotton et al., 2024b; Nayana et al., 2024). Also, observation of these filaments overlying on top of each other in the north-west could indicate that shock waves are progressing outwards through an environment with uniform low density. The complexity in explaining the G7.7-3.7 blowout phenomenon seeks multi-wavelength study.

4.4 Constraining the Age of G7.7-3.7

The current age of G7.7-3.7, 1.2 ± 0.6 kyrs, was inferred from the ionization timescale of a shocked plasma in the south blowout from the X-ray observation (Zhou et al., 2018). This age could be associated with huge errors as it was under the assumption that the shocked plasma had not reached ionization equilibrium. In this study, we employ the expansion rate of G7.7-3.7 from the expansion measured between two radio observations to calculate the age and shock speed (Allen et al., 2015). We used our MeerKAT data and VLA data for an observation at a beam size of $71'' \times 35''$ on February 23 1991 (Dubner et al., 1996).

MeerKAT data was convolved to have the same beam size as VLA data using CASA task imsmooth. The measured MeerKAT and VLA angular radius were $\theta_{MeerKAT} \simeq 0°.214 \pm 0.0001$ and $\theta_{VLA} \simeq 0°.211 \pm 0.0001$ respectively. The mean amount of expansion of G7.7-3.7 is $\Delta\theta \simeq 9 \pm 0.45$ arcsec over a period of Δt = 31.907 yr corresponding to an expansion rate $\dot{\theta} \simeq 0.282 \pm 0.014$ arcsec yr^{-1}. The fractional expansion rate, $\dot{\theta}/\theta$, can be used to give a constraint on the age of G7.7-3.7. The shock radius, r, is related to age, t, by $r \; \alpha \; t^m$ where m is an expansion parameter (Allen et al., 2015; Aschenbach et al., 1999). If m is a constant over the time duration of expansion, then age will be $t = m\theta/\dot{\theta}$. The value of m is not clearly known for G7.7-3.7, however, most likely it is within the range between 0.4 (Sedov-Taylor phase) and 1 (free-expansion phase) (Allen et al., 2015).

In this case, G7.7-3.7 with an angular radius of $\theta \simeq 769$ arcsecs will have an age $\sim$ 1090 ± 77 yrs if it is in Sedov-Taylor phase or $\sim$ 2726 ± 192 yrs if it is still in free-expansion phase. G7.7-3.7 could be in the Sedov-Taylor phase with its age $\geq$ 1000 yrs which is in the range of the age of the shocked plasma which was studied in the southern blowout in X-ray observation (Zhou et al., 2018). Moreover, adjusting for a more realistic value for the parameter m = 0.6, the revised age estimate was calculated to be 1636 ± 115 yrs, which fits better with the explosion event of 386 CE and the observed data in 2023.

The shock speed, v, can be given by $v = 4.741\dot{\theta}d$ where, $\dot{\theta}$ is expansion rate in arcsec yr^{-1}, d is the distance to the remnant in pc and 4.741 is units conversion factor to km s^{-1} (Acord et al., 1998; Aschenbach et al., 1999). In this work, we adopted the latest distance to G7.7-3.7 of 4.4 kpc (Pavlović et al., 2013) and got a shock speed of 5883 ± 294 km s^{-1}. With interest to compare the shock speed of G7.7-3.7 with other remnants, we plotted it's velocity against age alongside other supernova remnants and their distances as shown in Figure 4.3. It is clear that most of the young remnants with ages up to around 1200 yrs

have high shock speed ranging between ~ 3000 km s^{-1} to ~ 8000 km s^{-1}. On contrary, old remnants with ages > 1200 yrs have low shock speed < 2000 km s^{-1}.

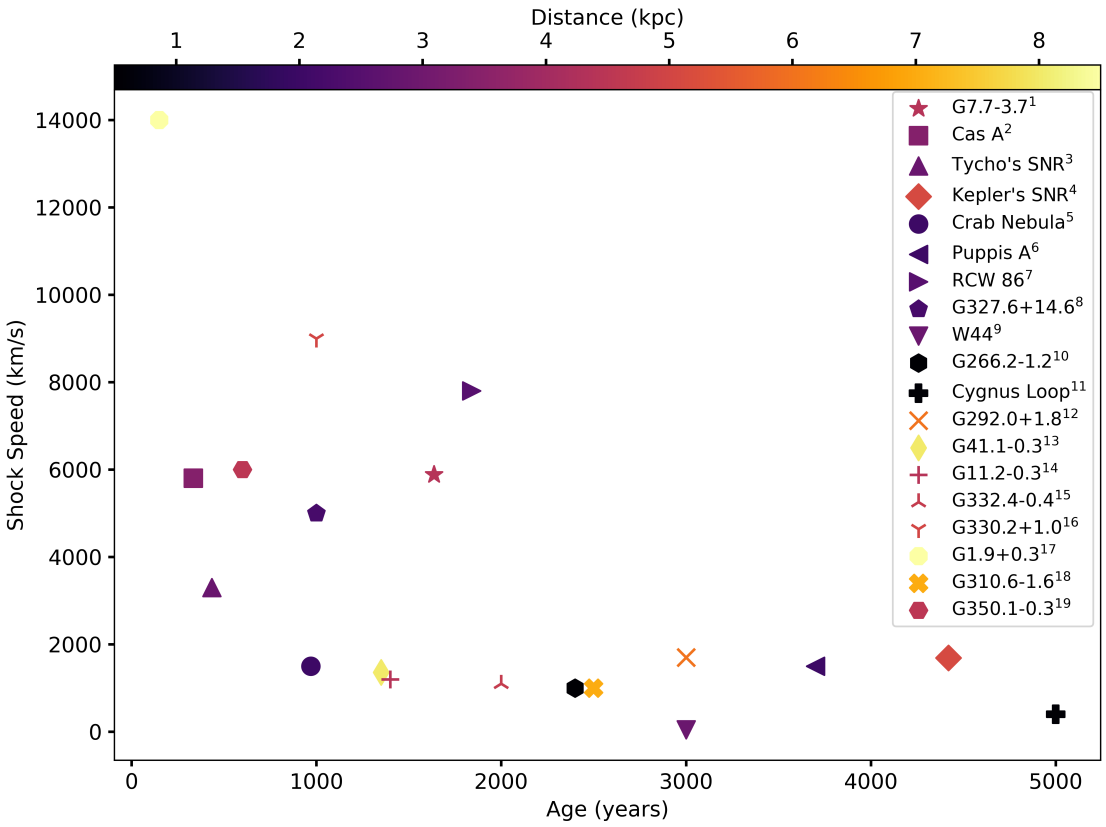

Figure 4.3: The relationship between shock speed and age for G7.7-3.7 versus other SNRs. The color bar shows the distances to the SNRs. The references where these values were taken from are: 1. this paper; Pavlović et al. (2013), 2. Orlando et al. (2022), Picquenot et al. (2024), Reed et al. (1995), and Vink et al. (2022), 3. Petruk et al. (2024), Picquenot et al. (2024), Ruiz-Lapuente (2004), and Völk et al. (2008), 4. Picquenot et al. (2024), Sankrit et al. (2016), and Sapienza et al. (2024), 5. Bietenholz et al. (1991), Clark et al. (1983), and Yang and Chevalier (2015), 6. Ghavamian et al. (2024), Winkler and Kirshner (1985), and Winkler et al. (1988), 7. Broersen et al. (2014) and Williams et al. (2011), 8. Jiang and Zhao (2007) and Katsuda et al. (2013), 9. Anderl et al. (2014), 10. Allen et al. (2015), 11. Danforth et al. (2001), Raymond et al. (2020), and Salvesen et al. (2009), 12. Bhalerao et al. (2019) and Ghavamian et al. (2005), 13. Leahy and Ranasinghe (2016), 14. Borkowski et al. (2016), 15. Braun et al. (2019) and Carter et al. (1997), 16. Borkowski et al. (2018), 17. Borkowski et al. (2014), Brose et al. (2019), and Reynolds et al. (2008), 18. Reynolds and Borkowski (2019), 19. Borkowski et al. (2020)

4.5 G7.7-3.7 Multi-Wavelength Nature

Multi-wavelength nature of G7.7-3.7 was revealed from combination of radio emission together with X-ray and optical ones.

4.5.1 X-ray Emissions in G7.7-3.7

X-ray morphology of G7.7-3.7 as shown in Figure 4.4 revealed an arc-like structure in the south aligned in an east-west direction. There was a disparity between X-ray brightness along the arc-like structure with the intense X-ray emission toward east while less intense ones towards the west. Apart from the arc-like structure, there is an intense X-ray emitting spot in the north-eastern and faint emissions filling the rest of the interior part of the G7.7-3.7. Generally, bright X-ray emitting regions and spots of G7.7-3.7 are observed in the south and eastern side whereas very diffuse and faint ones fill the west and north-west side. The spectral line analysis from recent 2020 XMM observations (see Figure 4.5) shows the detected X-ray photons mainly have an energy <2 keV shown by emissions lines. A similar observation, to the 2012 one, of the He-like Si pump is shown at ~ 2KeV indicating a thermal origin of the emissions(Zhou et al., 2018). This energy distribution shows the presence of a heated shocked gas which could result in the release of X-ray emissions and the thermal emissions detected by the spectral index map in the south blowout.

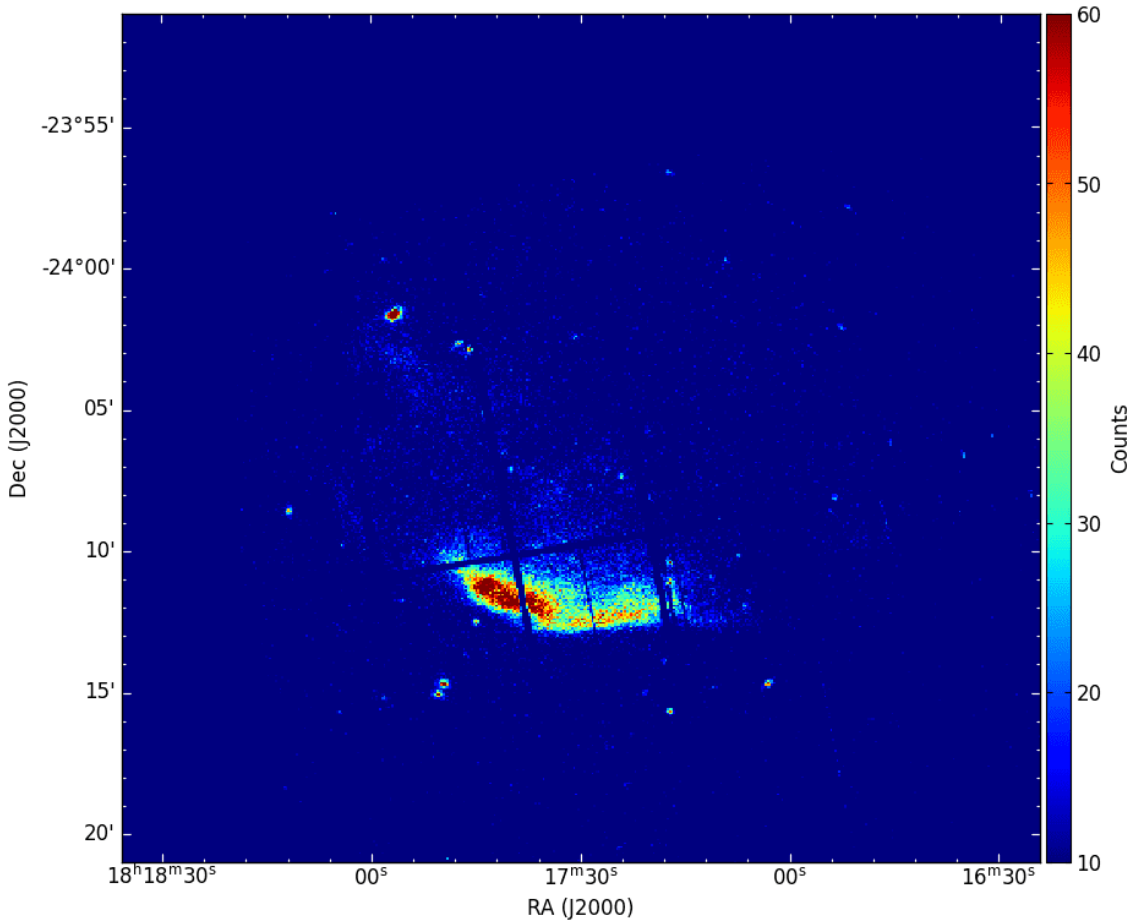

Figure 4.4: The XMM-Newton X-ray emissions in G7.7-3.7.

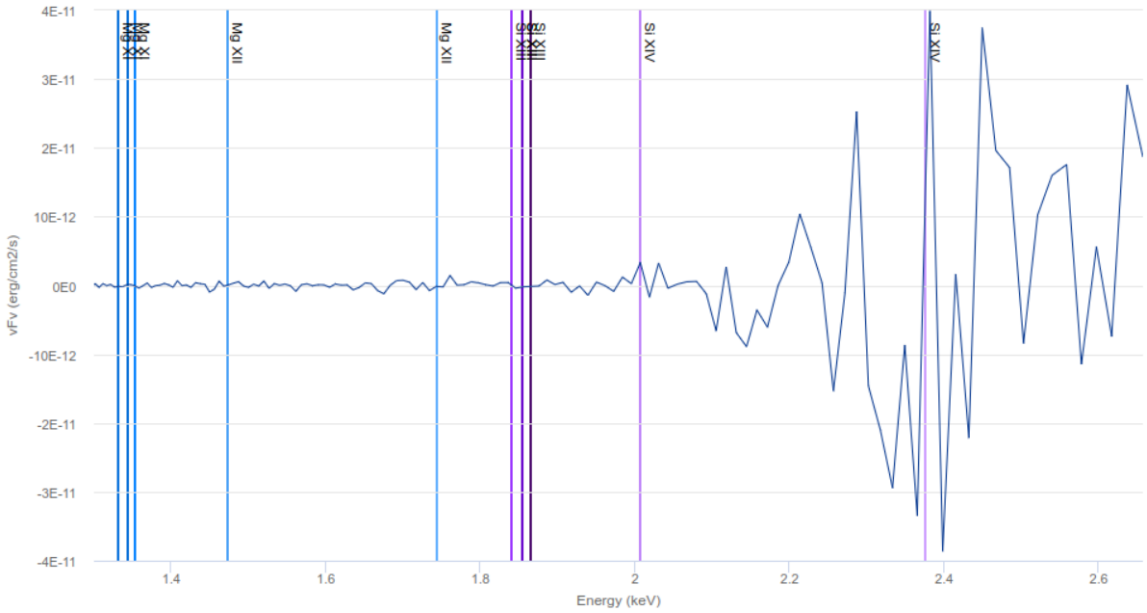

Figure 4.5: The X-ray energy distribution spectra of G7.7-3.7 visualization map with the detected spectral lines from X-ray observation in XMM - Newton Science Archive.

4.5.2 G7.7-3.7 Optical Emitting Region Cutout

The optical emitting region cutout of G7.7-3.7 is shown in the RGB image in Figure 4.6 for Hα + [NII] (red), [OIII] (green) and [SII] (blue) narrow-band filters. Two faint filament structures (labeled Filament A & B) were observed in Hα + [NII], [OIII] and marginally in [SII] narrow-band filters. These filaments are elongated in the east-west direction and are aligned with an X-ray arc-like feature and south radio blowout as shown in Figure 4.7. Filament A appears to be longer than Filament B. Filament A is more pronounced in optical emission, unlike Filament B.

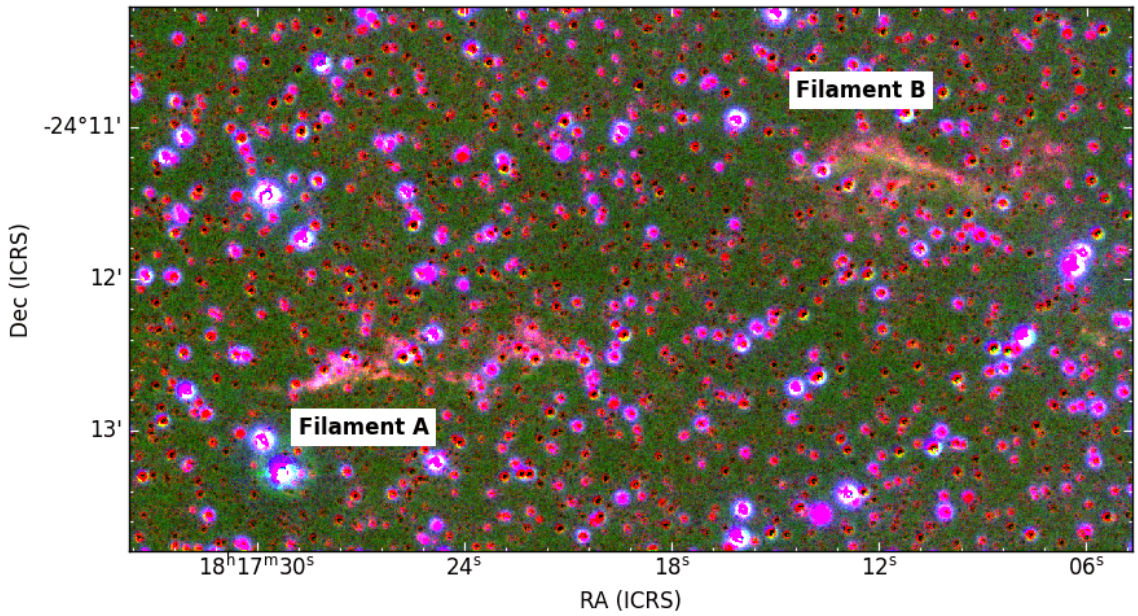

Figure 4.6: The RGB image (red - Hα + [NII], green - [OIII] and blue - [SII] narrow-band filters) showing Filaments A and B of G7.7-3.7 INT optical emitting region cutout from a dashed blue rectangle in Figure 4.7 (see fig. 1 & 2 in Domček et al. (2023)).

4.5.3 Combined Radio, X-ray and Optical Observation for G7.7-3.7

It was crucial to delve into multi-wavelength characteristics for a deep understanding of the fascinating nature of the G7.7-3.7 by combining radio observation (see Figure 4.1), X-ray observation (see Figure 4.4) and Optical observation (see Figure 4.6). Figure 4.7, provides a detailed mosaic image that captures G7.7-3.7 across various wavelengths, such

as radio (current work), X-ray (Zhou et al., 2018), and faint optical visible regions (Domček et al., 2023). G7.7-3.7 has a non-uniform distribution of X-ray emissions with the only bright arc-like feature in the southern radio blowout and the interior filled with diffuse X-ray emissions. Spectroscopic analysis of the southern arc-like feature showed that it comprised under-ionized shocked plasma with subsolar abundances. Zhou et al. (2018) suggested that G7.7-3.7 could likely be expanding into a low-density environment, which explains the observed low X-ray emissions. Furthermore, the ambient density appears to be non-uniform, as indicated by the non-spherical radio morphology and heightened X-ray emissions in the southern region.

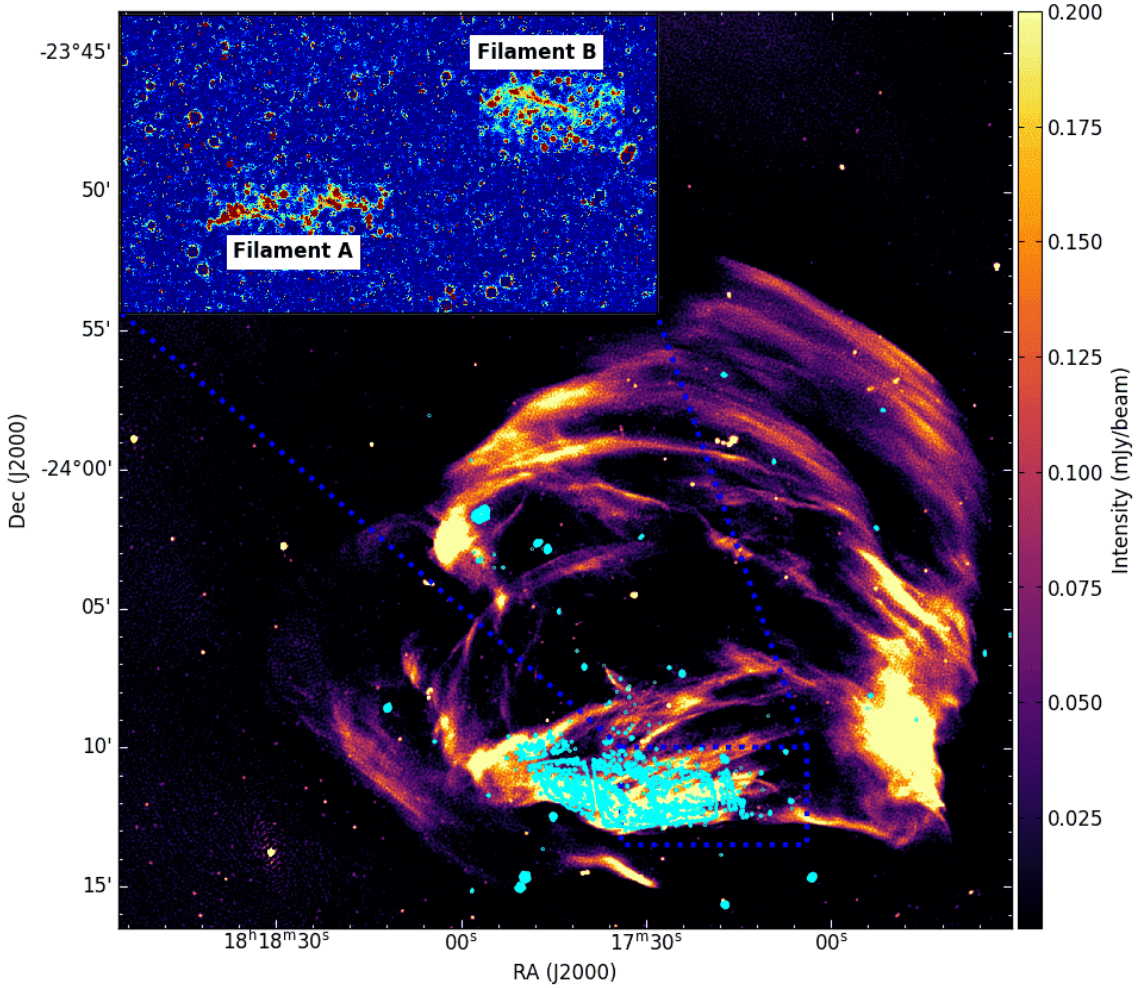

Figure 4.7: A mosaiced MeerKAT radio image of G7.7-3.7 (inferno) multi-wavelength structure. Cyan displays the XMM-Newton contours of G7.7-3.7 (see fig. 1 in Zhou et al. (2018)). The dashed blue rectangle displays a region with the INT detected faint optical emissions whose H α + [N II] image is projected at the top left corner (see fig. 1 & 2 in Domček et al. (2023)).

The optical observation of G7.7-3.7 in Hα + [N II], [O III], and marginally in [S II] narrow-band showed two faint filaments aligned with the X-ray south arc-like feature in the southern radio blowout. Long-slit spectroscopic analysis revealed a large ratio expected for shock-related remnants of [S II]/H $\alpha \simeq$ (1.6-2.5). Also, a large ratio of [N II]/H α > 2 showed that the gas in the south has high nitrogen particles. This is supported by the presence of nitrogen emission lines from the X-ray observation in Figure 4.5. Shocked gases that are nitrogen enriched showed the presence of circumstellar materials lost by the progenitor star. Thus, Domček et al. (2023) proposed that the G7.7-3.7 forward shock collides with a locally high-density circumstellar shell lying in the south resulting in the formation of optical filaments.

The comprehensive study across multiple wavelengths (see Figure 4.7) reveals the southern radio blowout as a captivating blowout. This blowout shows a coincidence of features in radio blowout, bright X-ray emission, and two faint optical filaments aligned with the X-ray bright arc. The key inquiry revolves around the origin of this brightness coincidence in the southern blowout across the three wavelengths. The possibility of mass outflows due to weakening in magnetic fields, by Cotton et al. (2024b), at certain regions along its perimeter could result in blowouts in radio observations. Forward shock fronts create localized blowouts with high densities of shocked particles resulting in non-uniform mass outflows with localized knots of bright synchrotron radio emissions and few traces of thermal emissions.

Alternatively, these blowouts are related to the mass outflows and their distinct position could be explained by the way the explosion occurred resulting in non-uniform mass outflow. The explosion could have occurred in such a way that the large clump of masses was deposited in the south, a less massive one in the east with the remaining very massive

one deposited in the west. These clumps of masses result in the formation of localized intense radio emissions in the blowouts from the high population of ionized particles in those clumps. It looks like the explosion occurred toward the southern and eastern directions and the remaining masses moved slowly in the west while the north-west direction was filled with masses connecting the eastern mass and the remaining western mass.

Additionally, the strong blast wave could be directed toward the southern and eastern directions unlike west and north-west directions resulting in the formation of intense X-ray emissions in those regions after colliding with ISM (see Figure 4.4 or 4.7), whereas fainter ones in the west and north-west. Finally, the surrounding environment could be composed of non-uniformly distributed low-density ISM (Zhou et al., 2018). The non-uniformly distributed low-density ISM resulted in the formation of not a perfect spherical structure in radio observation and faint X-ray emissions in the west and north-west. Despite this, the presence of high-density shells in the south results in the formation of intense X-ray emissions after colliding with blast waves and stretching of the south blowout in radio observation. Additionally, the composition of this high-density shell with the circumstellar materials, as found by Domček et al. (2023), results in the formation of faint optical filaments (see Figure 4.6 or 4.7) from the collision of blast waves with circumstellar materials.

CHAPTER FIVE: CONCLUSION, RECOMMENDATION AND PUBLICATION

5.1 Conclusion

We presented the MeerKAT radio observations of G7.7-3.7 at 1284 MHz to examine its radio structure at a higher resolution and its multi-wavelength nature. We found that G7.7-3.7 is an almost circular structure with filamentary structures in radio observation. G7.7-3.7 has a strong bright blowout in the western boundary and extended bright filament in the southern perimeter with feather-like filaments which seem disconnected from the western bright blowout. The eastern has a faint blowout with a bright point source at the center. The north-west is occupied by faint elongated filaments connecting the eastern point source and the western bright blowout. We suggest that the blowouts originate from the non-uniform mass outflow from the localized high-density population of the shock-accelerated particles and the weakening of magnetic fields along its perimeter.

The spectral index distribution map of G7.7-3.7 revealed unique features with a fluctuating spectrum, ranging $\alpha \sim 0$ to $\sim$ -3, suggesting strong synchrotron emissions with faint traces of thermal emissions for values towards $\alpha \sim 0$ mostly at the edges of the bright blowouts. The bright blowouts have less steep spectral indices ranging $\sim$ -0.5 to $\sim$ -1.5, while the dimmer and more diffuse filaments show very steep spectral indices, $\alpha \sim$ -3. Bright blowouts with a less steep spectrum are dominated by shock-accelerated particles encountering irregularities and weakening in magnetic fields. However, the faint emissions along the filaments connecting the eastern and western blowouts with a very steep spectral index of $\sim$ -3 comprises synchrotron emissions from aged particles that have dissipated a lot of energy due to turbulent re-acceleration.

Analysis of MeerKAT and VLA data gives the mean amount of expansion of G7.7-3.7 is $\Delta\theta$ = 9 ± 0.45 arcsec over a period of Δt = 31.907 yr corresponding to an expansion rate $\dot{\theta}$ = 0.282 ± 0.014 arcsec yr^{-1} corresponding to a shock speed of 5883 ± 294 km s^{-1}. This expansion rate for m = 0.6, gives the revised age to be 1636 ± 115 yrs, which fits better with the explosion event of 386 CE and the observed data in 2023. This age is in the range of the shocked plasma age that was studied in the southern blowout in X-ray observation. The age estimates derived from expansion rate analysis provide independent constraints on the remnant's age and do not assume an earlier definitive link to SN 386.

The G7.7-3.7 multi-wavelength study revealed captivating attention in the southern radio blowout. This blowout exhibits a coincidence of features, including a radio blowout, a bright X-ray arc, and two faint optical filaments aligned with the X-ray arc. The collision of the shock front with ISM results in X-ray emissions while with the circumstellar materials results in faint optical filaments. G7.7-3.7 is likely expanding in a low-density environment and colliding with ISM. The low-density ISM could result in the formation of faint synchrotron filament emissions progressing uniformly in the north-west and also, diffuse and faint X-ray emissions in the interior of G7.7-3.7. The non-uniform ISM density distribution could result in a not-so-spherical radio structure. The presence of a high-density wall/shell could result in traces of thermal emissions in radio and intense X-ray emissions in the south. The composition of this high-density wall/shell with circumstellar materials from the progenitor star could result in the formation of an optical filament still in the south and intense X-ray emissions from shock-heated gas.

5.2 Recommendation

Although our findings shed light on the complex interplay of physical processes (such as age, shock speed and multi-wavelength structure) within G7.7-3.7, offering valuable in-

sights into the dynamics and evolution of supernova remnants, investigations in other wavelengths like infrared and ultraviolet may blend the structural studies of G7.7-3.7. Observations of the column density distributions around G7.7-3.7 may assess density variations predicted in this work. Additionally, detailed hydrodynamic simulations are required to assess the observations of G7.7-3.7.

5.3 Publication

"MeerKAT-Based Multi-Wavelength Study of Supernova Remnant G7.7-3.7 (SN 386?)" DOI: 10.1016/j.newast.2025.102370[6]. Authored by Patrick N. Mwaniki, James O. Chibueze and Dismas S. Wamalwa (Mwaniki et al., 2025). This paper was submitted and published by New Astronomy[7] journal. The full paper is attached in Appendix H.

The results were presented in XXXII International Astronomical Union (IAU) general assembly[8] in Cape Town, South Africa, see Mwaniki et al. (2024) [9]. The poster[10] is attached in Appendix G.

[6]https://doi.org/10.1016/j.newast.2025.102370
[7]https://www.sciencedirect.com/journal/new-astronomy
[8]https://astronomy2024.org/
[9]https://ui.adsabs.harvard.edu/abs/2024IAUGA..32P.669M
[10]https://ui.adsabs.harvard.edu/abs/2024IAUGA..32P.669M

REFERENCES

Acero, F., Ackermann, M., Ajello, M., Baldini, L., Ballet, J., Barbiellini, G., Bastieri, D., Bellazzini, R., Bissaldi, E., Blandford, R. D., Bloom, E. D., Bonino, R., Bottacini, E., Brandt, T. J., Bregeon, J., Bruel, P., Buehler, R., Buson, S., Caliandro, G. A., … Zimmer, S. (2016). The First Fermi LAT Supernova Remnant Catalog. ApJS, 224(1), Article 8, 8. https://doi.org/10.3847/0067-0049/224/1/8

Acord, J., Churchwell, E, & Wood, D. (1998). The expansion rate of and distance to g5. 89–0.39. The Astrophysical Journal, 495(2), L107.

Allen, G. E., Chow, K., DeLaney, T., Filipović, M. D., Houck, J. C., Pannuti, T. G., & Stage, M. D. (2015). On the Expansion Rate, Age, and Distance of the Supernova Remnant G266.2-1.2 (Vela Jr.) ApJ, 798(2), Article 82, 82. https://doi.org/10.1088/0004-637X/798/2/82

Anderl, S., Gusdorf, A., & Güsten, R. (2014). APEX observations of supernova remnants. I. Non-stationary magnetohydrodynamic shocks in W44. A&A, 569, Article A81, A81. https://doi.org/10.1051/0004-6361/201423561

Arendt, R. G. (1989). An Infrared Survey of Galactic Supernova Remnants. ApJS, 70, 181. https://doi.org/10.1086/191337

Arias, M., Zhou, P., Chiotellis, A., De Breuck, C., Domcek, V., Boumis, P., Vink, J., Derlopa, S., & Akras, S. (2024). Two shell- and wing-shaped supernova remnants. Investigating the molecular environments around VRO 42.05.01 and G 350.0-2.0. arXiv e-prints, Article arXiv:2402.10763, arXiv:2402.10763. https://doi.org/10.48550/arXiv.2402.10763

Aschenbach, B., Iyudin, A. F., & Schönfelder, V. (1999). Constraints of age, distance and progenitor of the supernova remnant RX J0852.0-4622/GRO J0852-4642. A&A, 350, 997–1006. https://doi.org/10.48550/arXiv.astro-ph/9909415

Astropy Collaboration, Robitaille, T. P., Tollerud, E. J., Greenfield, P., Droettboom, M., Bray, E., Aldcroft, T., Davis, M., Ginsburg, A., Price-Whelan, A. M., Kerzendorf, W. E., Conley, A., Crighton, N., Barbary, K., Muna, D., Ferguson, H., Grollier, F., Parikh, M. M., Nair, P. H., … Streicher, O. (2013). Astropy: A community Python package for astronomy. A&A, 558, Article A33, A33. https://doi.org/10.1051/0004-6361/201322068

Ball, B. D., Kothes, R., Rosolowsky, E., West, J., Becker, W., Filipović, M. D., Gaensler, B. M., Hopkins, A. M., Koribalski, B., Landecker, T., Leahy, D., Marvil, J., Sun, X., Bufano, F., Carretti, E., Ingallinera, A., Van Eck, C. L., & Willis, T. (2023). A catalogue of radio supernova remnants and candidate supernova remnants in the EMU/POSSUM Galactic pilot field. MNRAS, 524(1), 1396–1421. https://doi.org/10.1093/mnras/stad1953

Benaglia, P. (2024). Stars, bow shocks, and gamma-ray sources. arXiv e-prints, Article arXiv:2402.10623, arXiv:2402.10623. https://doi.org/10.48550/arXiv.2402.10623

Bhalerao, J., Park, S., Schenck, A., Post, S., & Hughes, J. P. (2019). Detailed X-Ray Mapping of the Shocked Ejecta and Circumstellar Medium in the Galactic Core-collapse Supernova Remnant G292.0+1.8. ApJ, 872(1), Article 31, 31. https://doi.org/10.3847/1538-4357/aafafd

Bietenholz, M. F., Kronberg, P. P., Hogg, D. E., & Wilson, A. S. (1991). The Expansion of the Crab Nebula. ApJ, 373, L59. https://doi.org/10.1086/186051

Booth, R. S., de Blok, W. J. G., Jonas, J. L., & Fanaroff, B. (2009). MeerKAT Key Project Science, Specifications, and Proposals. arXiv e-prints, Article arXiv:0910.2935, arXiv:0910.2935. https://doi.org/10.48550/arXiv.0910.2935

Booth, R. S., & Jonas, J. L. (2012). An Overview of the MeerKAT Project. African Skies, 16, 101.

Booth, R., Goedhart, S., & Jonas, J. MeerKAT and its potential for Cosmic MASER Research (R. S. Booth, W. H. T. Vlemmings, & E. M. L. Humphreys, Eds.). In: Cosmic masers - from oh to h0 (R. S. Booth, W. H. T. Vlemmings, & E. M. L. Humphreys, Eds.). Ed. by Booth, R. S., Vlemmings, W. H. T., & Humphreys, E. M. L. 287. 2012, July, 483–487. https://doi.org/10.1017/S1743921312007569

Borkowski, K. J., Miltich, W., & Reynolds, S. P. (2020). Expansion and Age of the Supernova Remnant G350.1-0.3: High-velocity Iron Ejecta from a Core-collapse Event. ApJ, 905(2), Article L19, L19. https://doi.org/10.3847/2041-8213/abcda7

Borkowski, K. J., Reynolds, S. P., Green, D. A., Hwang, U., Petre, R., Krishnamurthy, K., & Willett, R. (2014). Nonuniform Expansion of the Youngest Galactic Supernova Remnant G1.9+0.3. ApJ, 790(2), Article L18, L18. https://doi.org/10.1088/2041-8205/790/2/L18

Borkowski, K. J., Reynolds, S. P., & Roberts, M. S. E. (2016). G11.2-0.3: The Young Remnant of a Stripped-envelope Supernova. ApJ, 819(2), Article 160, 160. https://doi.org/10.3847/0004-637X/819/2/160

Borkowski, K. J., Reynolds, S. P., Williams, B. J., & Petre, R. (2018). Expansion and Age of the X-Ray Synchrotron-dominated Supernova Remnant G330.2+1.0. ApJ, 868(2), Article L21, L21. https://doi.org/10.3847/2041-8213/aaedb5

Boumis, P., Chiotellis, A., Fragkou, V., Akras, S., Derlopa, S., Kopsacheili, M., Leonidaki, I., Alikakos, J., Palaiologou, E. V., Harvey, E., & Souropanis, D. (2022). Deep optical study of the mixed-morphology supernova remnant G 132.7+1.3 (HB3). MNRAS, 512(2), 1658–1676. https://doi.org/10.1093/mnras/stac412

Braun, C., Safi-Harb, S., & Fryer, C. L. (2019). Progenitors and explosion properties of supernova remnants hosting central compact objects: I. RCW 103 associated with the peculiar source 1E 161348-5055. MNRAS, 489(3), 4444–4463. https://doi.org/10.1093/mnras/stz2437

Bresci, V., Lemoine, M., & Gremillet, L. (2023). Particle acceleration at magnetized, relativistic, turbulent shock fronts. Physical Review Research, 5(2), Article 023194, 023194. https://doi.org/10.1103/PhysRevResearch.5.023194

Broersen, S., Chiotellis, A., Vink, J., & Bamba, A. (2014). The many sides of RCW 86: a Type Ia supernova remnant evolving in its progenitor's wind bubble. MNRAS, 441(4), 3040–3054. https://doi.org/10.1093/mnras/stu667

Brose, R., Sushch, I., Pohl, M., Luken, K. J., Filipović, M. D., & Lin, R. (2019). Non-thermal emission from the reverse shock of the youngest Galactic supernova remnant G1.9+0.3. A&A, 627, Article A166, A166. https://doi.org/10.1051/0004-6361/201834430

Camilo, F. (2018). African star joins the radio astronomy firmament. Nature Astronomy, 2(7), 594–594.

Carter, L. M., Dickel, J. R., & Bomans, D. J. (1997). Expansion of the Supernova Remnant RCW 103. PASP, 109, 990–997. https://doi.org/10.1086/133971

Case, G., & Bhattacharya, D. (1996). Revisiting the galactic supernova remnant distribution. A&AS, 120, 437–440.

Chevalier, R. A., & Fransson, C. (2006). Circumstellar Emission from Type Ib and Ic Supernovae. ApJ, 651(1), 381–391. https://doi.org/10.1086/507606

Chibueze, J. O., Caleb, M., Spitler, L., Ashkar, H., Schüssler, F., Stappers, B. W., Venter, C., Heywood, I., Richards, A. M. S., Williams, D. R. A., Kramer, M., Beswick, R., Bezuidenhout, M. C., Breton, R. P., Driessen, L. N., Jankowski, F., Keane, E. F., Malenta, M., Mickaliger, M., … Żywucka, N. (2022). A MeerKAT, e-MERLIN, H.E.S.S., and Swift search for persistent and transient emission associated with three localized FRBs. MNRAS, 515(1), 1365–1379. https://doi.org/10.1093/mnras/stac1601

Clark, D. H., Murdin, P., Wood, R., Gilmozzi, R., Danziger, J., & Furr, A. W. (1983). Three dimensional structure of the Crab nebula. MNRAS, 204, 415–431. https://doi.org/10.1093/mnras/204.2.415

Cotton, W. D., Filipović, M. D., Camilo, F., Indebetouw, R., Alsaberi, R. Z. E., Anih, J. O., Baker, M., Bastian, T. S., Bojičić, I., Carli, E., Cavallaro, F., Crawford, E. J., Dai, S., Haberl, F., Levin, L., Luken, K., Pennock, C. M., Rajabpour, N., Stappers, B. W., … Serylak, M. (2024a). The MeerKAT 1.3 GHz Survey of the Small Magellanic Cloud. MNRAS, 529(3), 2443–2472. https://doi.org/10.1093/mnras/stae277

Cotton, W. D., Kothes, R., Camilo, F., Chandra, P., Buchner, S., & Nyamai, M. (2024b). MeerKAT 1.3 GHz Observations of Supernova Remnants. ApJS, 270(2), Article 21, 21. https://doi.org/10.3847/1538-4365/ad0ecb

Danforth, C. W., Blair, W. P., & Raymond, J. C. (2001). A Detailed Analysis of a Cygnus Loop Shock-Cloud Interaction. AJ, 122(2), 938–953. https://doi.org/10.1086/321161

de Villiers, M. S. (2023). MeerKAT Holography Measurements in the UHF, L, and S Bands. AJ, 165(3), Article 78, 78. https://doi.org/10.3847/1538-3881/acabc3

Dickel, J. R., & Milne, D. K. (1976). Magnetic fields in supernova remnants. Australian Journal of Physics, 29, 435–460. https://doi.org/10.1071/PH760435

Domček, V., Hernández Santisteban, J. V., Chiotellis, A., Boumis, P., Vink, J., Akras, S., Souropanis, D., Zhou, P., & de Burgos, A. (2023). Detection of optical emission from the supernova remnant G7.7-3.7. MNRAS, 526(1), 1112–1121. https://doi.org/10.1093/mnras/stad2779

Dubner, G. (2008). Supernova remnants: A link between massive stars and the surrounding medium. Revista Mexicana de Astronomía y Astrofísica, 33, 148–153.

Dubner, G. Radio emision from supernova remnants. In: In Supernova remnants: An odyssey in space after stellar death. 2016, June, 79, 79.

Dubner, G. M., Giacani, E. B., Goss, W. M., Moffett, D. A., & Holdaway, M. (1996). VLA Observations of Nine Galactic Supernova Remnants. AJ, 111, 1304. https://doi.org/10.1086/117875

Dubner, G., & Giacani, E. (2015). Radio emission from supernova remnants. A&ARv, 23, Article 3, 3. https://doi.org/10.1007/s00159-015-0083-5

Duvidovich, L., Petriella, A., Giacani, E., & Dubner, G. (2017). Supernova Remnants associated with high energy sources. Boletin de la Asociacion Argentina de Astronomia La Plata Argentina, 59, 136–138.

Fesen, R. A., Drechsler, M., Strottner, X., Falls, B., Sainty, Y., Martino, N., Galli, R., Ludgate, M., Blauensteiner, M., Reich, W., Walker, S., di Cicco, D., Mittelman, D., Morgan, C., Ettahar Kaeouach, A., Rupert, J., & Benkhaldoun, Z. (2024). Deep Optical Emission-Line Images of Nine Known and Three New Galactic Supernova

Remnants. arXiv e-prints, Article arXiv:2403.00317, arXiv:2403.00317. https://doi.org/10.48550/arXiv.2403.00317

Gardner, F., Whiteoak, J., & Morris, D. (1969). The linear polarization of radio sources at 6 cm wavelength. Australian Journal of Physics, 22(6), 821–838.

Ghavamian, P., Hughes, J. P., & Williams, T. B. (2005). Exploring the Kinematics of the Oxygen-rich Supernova Remnant G292.0+1.8: Ejecta Shells, Fast-moving Knots, and Shocked Circumstellar Material. ApJ, 635(1), 365–380. https://doi.org/10.1086/497283

Ghavamian, P., Seitenzahl, I. R., Vogt, F. P. A., Raymond, J. C., & Scelsi, J. (2024). The Peculiar Ejecta Rings in the O-Rich Supernova Remnant Puppis A: Evidence of a Binary Interaction? ApJ, 960(1), Article 7, 7. https://doi.org/10.3847/1538-4357/ad0156

Giacani, E. Supernova remnants and their effects on the interstellar medium. In: In Revista mexicana de astronomia y astrofisica conference series. 49. Revista Mexicana de Astronomia y Astrofisica Conference Series. 2017, July, 43–44.

Green, D. A. (2014). A catalogue of 294 Galactic supernova remnants. Bulletin of the Astronomical Society of India, 42(2), 47–58. https://doi.org/10.48550/arXiv.1409.0637

Green, D. A. (2015). Constraints on the distribution of supernova remnants with Galactocentric radius. MNRAS, 454(2), 1517–1524. https://doi.org/10.1093/mnras/stv1885

Green, D. A. (2019). A revised catalogue of 294 Galactic supernova remnants. Journal of Astrophysics and Astronomy, 40(4), Article 36, 36. https://doi.org/10.1007/s12036-019-9601-6

Harris, C. R., Millman, K. J., Van Der Walt, S. J., Gommers, R., Virtanen, P., Cournapeau, D., Wieser, E., Taylor, J., Berg, S., Smith, N. J., et al. (2020). Array programming with numpy. Nature, 585(7825), 357–362.

Heywood, I. (2020, September). oxkat: Semi-automated imaging of MeerKAT observations.

Hickish, J., Abdurashidova, Z., Ali, Z., Buch, K. D., Chaudhari, S. C., Chen, H., Dexter, M., Domagalski, R. S., Ford, J., Foster, G., George, D., Greenberg, J., Greenhill, L., Isaacson, A., Jiang, H., Jones, G., Kapp, F., Kriel, H., Lacasse, R., … Werthimer, D. (2016). A Decade of Developing Radio-Astronomy Instrumentation using CASPER Open-Source Technology. Journal of Astronomical Instrumentation, 5(4), Article 1641001-12, 1641001–12. https://doi.org/10.1142/S2251171716410014

Hirashima, K., Moriwaki, K., Fujii, M. S., Hirai, Y., Saitoh, T. R., & Makino, J. (2023). 3D-Spatiotemporal forecasting the expansion of supernova shells using deep learning towards high-resolution galaxy simulations. MNRAS, 526(3), 4054–4066. https://doi.org/10.1093/mnras/stad2864

Holman, G. D. (2003). The effects of low- and high-energy cutoffs on solar flare microwave and hard x-ray spectra. The Astrophysical Journal, 586(1), 606. https://doi.org/10.1086/367554

Huang, Z.-Q., Reville, B., Kirk, J. G., & Giacinti, G. (2023). Prospects for ultra-high-energy particle acceleration at relativistic shocks. MNRAS, 522(4), 4955–4962. https://doi.org/10.1093/mnras/stad1356

Hunter, J. D. (2007). Matplotlib: A 2d graphics environment. Computing in science & engineering, 9(03), 90–95.

Jarvis, M. J. (2012). Multi-wavelength Extragalactic Surveys and the Role of MeerKAT and SALT. African Skies, 16, 44. https://doi.org/10.48550/arXiv.1107.5165

Jiang, S.-Y., & Zhao, F.-Y. (2007). The Historical Re-Brightening and Distance Recheck of SN 1006. Chinese J. Astron. Astrophys. 7(2), 325–328. https://doi.org/10.1088/1009-9271/7/2/17

Jonas, J., & MeerKAT Team. The MeerKAT Radio Telescope. In: In Meerkat science: On the pathway to the ska. 2016, January, 1, 1. https://doi.org/10.22323/1.277.0001

Jonas, J. L. (2009). MeerKAT - The South African Array With Composite Dishes and Wide-Band Single Pixel Feeds. IEEE Proceedings, 97(8), 1522–1530. https://doi.org/10.1109/JPROC.2009.2020713

Joye, W. A., & Mandel, E. New Features of SAOImage DS9 (H. E. Payne, R. I. Jedrzejewski, & R. N. Hook, Eds.). In: Astronomical data analysis software and systems xii (H. E. Payne, R. I. Jedrzejewski, & R. N. Hook, Eds.). Ed. by Payne, H. E., Jedrzejewski, R. I., & Hook, R. N. 295. Astronomical Society of the Pacific Conference Series. 2003, January, 489.

Kaplan, D. L., Condon, J. J., Arzoumanian, Z., & Cordes, J. M. (1998). Pulsars in the NRAO VLA Sky Survey. ApJS, 119(1), 75–82. https://doi.org/10.1086/313153

Katsuda, S., Long, K. S., Petre, R., Reynolds, S. P., Williams, B. J., & Winkler, P. F. (2013). X-Ray Proper Motions and Shock Speeds along the Northwest Rim of SN 1006. ApJ, 763(2), Article 85, 85. https://doi.org/10.1088/0004-637X/763/2/85

Kenyon, J. S., Smirnov, O. M., Grobler, T. L., & Perkins, S. J. (2018). CUBICAL - fast radio interferometric calibration suite exploiting complex optimization. MNRAS, 478(2), 2399–2415. https://doi.org/10.1093/mnras/sty1221

Kirchschlager, F., Sartorio, N. S., De Looze, I., Barlow, M. J., Schmidt, F. D., & Priestley, F. D. (2024). From total destruction to complete survival: dust processing at different evolutionary stages in the supernova remnant Cassiopeia A. MNRAS, 528(3), 5364–5376. https://doi.org/10.1093/mnras/stae365

Kirk, J. G., Reville, B., & Huang, Z.-Q. (2023). Particle acceleration at ultrarelativistic, perpendicular shock fronts. MNRAS, 519(1), 1022–1029. https://doi.org/10.1093/mnras/stac3589

Kochanek, C. S., Raymond, J. C., & Caldwell, N. (2024). The Distance to the S147 Supernova Remnant. arXiv e-prints, Article arXiv:2403.13892, arXiv:2403.13892. https://doi.org/10.48550/arXiv.2403.13892

Kopsacheili, M., Jiménez-Palau, C., Galbany, L., Boumis, P., & González-Díaz., R. (2024). Supernova remnant properties and luminosity functions in NGC 7793 using MUSE IFS. MNRAS, 530(1), 1078–1117. https://doi.org/10.1093/mnras/stae874

Kumari, S., & Pal, S. (2024). Discovery of a circularly symmetric extended diffuse radio emission around an elliptical galaxy with the VLA FIRST survey. MNRAS, 527(4), 11233–11239. https://doi.org/10.1093/mnras/stad3953

Leahy, D. A., & Ranasinghe, S. (2016). Distance and Evolutionary State of the Supernova Remnant 3C 397 (G41.1-0.3). ApJ, 817(1), Article 74, 74. https://doi.org/10.3847/0004-637X/817/1/74

Leahy, D. A., Merrick, F., & Filipović, M. (2022). Radio Emission from Supernova Remnants: Model Comparison with Observations. Universe, 8(12), 653. https://doi.org/10.3390/universe8120653

Long, K. S. Galactic and Extragalactic Samples of Supernova Remnants: How They Are Identified and What They Tell Us (A. W. Alsabti & P. Murdin, Eds.). In: Handbook of supernovae (A. W. Alsabti & P. Murdin, Eds.). Ed. by Alsabti, A. W., & Murdin, P. 2017, p. 2005. https://doi.org/10.1007/978-3-319-21846-5_90

Lovell, J. B., Keating, G. K., Wilner, D. J., Andrews, S. M., MacGregor, M., Rahman, R. A., Rao, R., & Williams, J. P. (2024). SMA Detection of an Extreme Millimeter Flare from the Young Class III Star HD 283572. ApJ, 962(1), Article L12, L12. https://doi.org/10.3847/2041-8213/ad18ba

Mantovanini, S., Becker, W., Khokhriakova, A., Hurley-Walker, N., Anderson, G. E., & Nicastro, L. (2024). G321.3-3.9: a new supernova remnant observed with multi-band radio data and in the SRG/eROSITA All-Sky Surveys. arXiv e-prints, Article arXiv:2401.17294, arXiv:2401.17294. https://doi.org/10.48550/arXiv.2401.17294

Martinez, J. R., del Palacio, S., & Bosch-Ramon, V. (2023). Probing the non-thermal physics of stellar bow shocks using radio observations. A&A, 680, Article A99, A99. https://doi.org/10.1051/0004-6361/202347720

Mauch, T., Cotton, W. D., Condon, J. J., Matthews, A. M., Abbott, T. D., Adam, R. M., Aldera, M. A., Asad, K. M. B., Bauermeister, E. F., Bennett, T. G. H., Bester, H., Botha, D. H., Brederode, L. R. S., Brits, Z. B., Buchner, S. J., Burger, J. P., Camilo, F., Chalmers, J. M., Cheetham, T., … Xaia, B. (2020). The 1.28 GHz MeerKAT DEEP2 Image. ApJ, 888(2), Article 61, 61. https://doi.org/10.3847/1538-4357/ab5d2d

McMullin, J. P., Waters, B., Schiebel, D., Young, W., & Golap, K. CASA Architecture and Applications (R. A. Shaw, F. Hill, & D. J. Bell, Eds.). In: Astronomical data analysis software and systems xvi (R. A. Shaw, F. Hill, & D. J. Bell, Eds.). Ed. by Shaw, R. A., Hill, F., & Bell, D. J. 376. Astronomical Society of the Pacific Conference Series. 2007, October, 127.

Miceli, M. (2023). Plasma heating and particle acceleration in collisionless shocks through astrophysical observations. Plasma Physics and Controlled Fusion, 65(3), Article 034003, 034003. https://doi.org/10.1088/1361-6587/acb082

Michailidis, M., Pühlhofer, G., Santangelo, A., Becker, W., & Sasaki, M. (2024). X-ray counterpart detection and gamma-ray analysis of the SNR G279.0+01.1 with eROSITA and Fermi-LAT. arXiv e-prints, Article arXiv:2401.17311, arXiv:2401.17311. https://doi.org/10.48550/arXiv.2401.17311

Milne, D. K. (1987). An atlas of supernova remnant magnetic fields. Australian Journal of Physics, 40, 771–787. https://doi.org/10.1071/PH870771

Milne, D. K., & Dickel, J. R. (1974a). 2700 MHz polarization observations of 17 supernova remnants. Australian Journal of Physics, 27, 549–562. https://doi.org/10.1071/PH740549

Milne, D. K., & Dickel, J. R. (1975). 5 GHz polarization observations of 33 galactic radio sources. Australian Journal of Physics, 28, 209–230. https://doi.org/10.1071/PH750209

Milne, D. K., & Dickel, J. R. Radio Polarimetric Observations of Supernova Remnants (T. Gehrels, Ed.). In: Iau colloq. 23: Planets, stars, and nebulae: Studied with photopolarimetry (T. Gehrels, Ed.). Ed. by Gehrels, T. 1974, January, 1029.

Milne, D. K., Roger, R. S., Kesteven, M. J., Haynes, R. F., Wellington, K. J., & Stewart, R. T. (1986). G 7.7 - 3.7 - a supernova remnant with a high degree of radio polarization. MNRAS, 223, 487–495. https://doi.org/10.1093/mnras/223.3.487

Mwaniki, P. N., Chibueze, J. O., & Wamalwa, D. S. MeerKAT-Based Multi-Wavelength Study of Supernova Remnant SN386 (G7.7-3.7). In: In Iau general assembly. 2024, August, 669, 669.

Mwaniki, P. N., Chibueze, J. O., & Wamalwa, D. S. (2025). MeerKAT-based multi-wavelength study of supernova remnant G7.7-3.7 (SN386?) New Astron. 117, Article 102370, 102370. https://doi.org/10.1016/j.newast.2025.102370

Nayana, A. J., Anupama, G. C., Roy, N., Banerjee, D. P. K., Singh, K. P., Sonith, L. S., & Kamath, U. S. (2024). Shock-driven synchrotron radio emission from the 2021 outburst of RS Ophiuchi. arXiv e-prints, Article arXiv:2401.05643, arXiv:2401.05643. https://doi.org/10.48550/arXiv.2401.05643

Offringa, A. R., McKinley, B., Hurley-Walker, N., Briggs, F. H., Wayth, R. B., Kaplan, D. L., Bell, M. E., Feng, L., Neben, A. R., Hughes, J. D., Rhee, J., Murphy, T., Bhat, N. D. R., Bernardi, G., Bowman, J. D., Cappallo, R. J., Corey, B. E., Deshpande, A. A., Emrich, D., … Williams, C. L. (2014). WSCLEAN: an implementation of a fast, generic wide-field imager for radio astronomy. MNRAS, 444(1), 606–619. https://doi.org/10.1093/mnras/stu1368

Orlando, S., Wongwathanarat, A., Janka, H. T., Miceli, M., Nagataki, S., Ono, M., Bocchino, F., Vink, J., Milisavljevic, D., Patnaude, D. J., & Peres, G. (2022). Evidence for past interaction with an asymmetric circumstellar shell in the young SNR Cassiopeia A. A&A, 666, Article A2, A2. https://doi.org/10.1051/0004-6361/202243258

Parker, Q. A., Phillipps, S., Pierce, M. J., Hartley, M., Hambly, N. C., Read, M. A., MacGillivray, H. T., Tritton, S. B., Cass, C. P., Cannon, R. D., Cohen, M., Drew, J. E., Frew, D. J., Hopewell, E., Mader, S., Malin, D. F., Masheder, M. R. W., Morgan, D. H., Morris, R. A. H., … Walker, R. N. F. (2005). The AAO/UKST SuperCOSMOS Hα survey. MNRAS, 362(2), 689–710. https://doi.org/10.1111/j.1365-2966.2005.09350.x

Pavlović, M. Z., Urošević, D., & Arbutina, B. (2018). Radio evolution of supernova remnants including non-linear particle acceleration. Nuclear and Particle Physics Proceedings, 297-299, 49–52. https://doi.org/10.1016/j.nuclphysbps.2018.07.007

Pavlović, M. Z., Urošević, D., Vukotić, B., Arbutina, B., & Göker, Ü. D. (2013). The Radio Surface-brightness-to-Diameter Relation for Galactic Supernova Remnants: Sample Selection and Robust Analysis with Various Fitting Offsets. ApJS, 204(1), Article 4, 4. https://doi.org/10.1088/0067-0049/204/1/4

Perek, L., & Kohoutek, L. (1967). Catalogue of Galactic Planetary Nebulae.

Petruk, O., Kuzyo, T., Patrii, M., Chomiuk, L., Arias, M., Miceli, M., Orlando, S., & Bocchino, F. (2024). Evidence of Gradients of Density and Magnetic Field in the Remnant of Tycho's Supernova. ApJ, 972(1), Article 63, 63. https://doi.org/10.3847/1538-4357/ad62ff

Picquenot, A., Holland-Ashford, T., & Williams, B. J. (2024). Comparing the three-dimensional morphological asymmetries in the ejecta of Kepler and Tycho in X-rays. A&A, 687, Article A28, A28. https://doi.org/10.1051/0004-6361/202449155

Rajpurohit, K., Lovisari, L., Botteon, A., Jones, C., Forman, W., O'Sullivan, E., van Weeren, R. J., HyeongHan, K., Bonafede, A., Jee, M. J., Vazza, F., Brunetti, G., Cho, H., Domínguez-Fernández, P., Stroe, A., Finner, K., Brüggen, M., Vrtilek, J. M., David, L. P., … De Gasperin, F. (2024). Abell 746: A Highly Disturbed Cluster Undergoing Multiple Mergers. ApJ, 966(1), Article 38, 38. https://doi.org/10.3847/1538-4357/ad29fa

Raymond, J. C., Chilingarian, I. V., Blair, W. P., Sankrit, R., Slavin, J. D., & Burkhart, B. (2020). Turbulence and Energetic Particles in Radiative Shock Waves in the Cygnus

Loop. I. Shock Properties. ApJ, 894(2), Article 108, 108. https://doi.org/10.3847/1538-4357/ab886d

Reed, J. E., Hester, J. J., Fabian, A. C., & Winkler, P. F. (1995). The Three-dimensional Structure of the Cassiopeia A Supernova Remnant. I. The Spherical Shell. ApJ, 440, 706. https://doi.org/10.1086/175308

Reyes-Iturbide, J., Ambrocio-Cruz, P., Silva, R., Rosado, M., Arias, L., Gabbasov, R., & Trigueros, D. (2024). The Galactic supernova remnant CTB 1: optical and X-ray emission analysis. MNRAS, 527(1), 803–812. https://doi.org/10.1093/mnras/stad3187

Reynolds, S. P., & Borkowski, K. J. (2019). On the Expansion, Age, and Origin of the Puzzling Shell/Pulsar-wind Nebula G310.6-1.6. ApJ, 887(2), Article 233, 233. https://doi.org/10.3847/1538-4357/ab5804

Reynolds, S. P., Borkowski, K. J., Green, D. A., Hwang, U., Harrus, I., & Petre, R. (2008). The Youngest Galactic Supernova Remnant: G1.9+0.3. ApJ, 680(1), L41. https://doi.org/10.1086/589570

Riseley, C. J., Bonafede, A., Bruno, L., Botteon, A., Rossetti, M., Biava, N., Bonnassieux, E., Loi, F., Vernstrom, T., & Balboni, M. (2024). A 'MeerKAT-meets-LOFAR' study of the complex multi-component (mini-)halo in the extreme sloshing cluster Abell 2142. arXiv e-prints, Article arXiv:2403.00414, arXiv:2403.00414. https://doi.org/10.48550/arXiv.2403.00414

Robitaille, T. (2019, February). APLpy v2.0: The Astronomical Plotting Library in Python (Version 2.0). Zenodo. https://doi.org/10.5281/zenodo.2567476

Romano, L. E. C., Behrendt, M., & Burkert, A. (2024). Cloud Formation by Supernova Implosion. arXiv e-prints, Article arXiv:2402.05796, arXiv:2402.05796. https://doi.org/10.48550/arXiv.2402.05796

Ruiz-Lapuente, P. (2004). Tycho Brahe's Supernova: Light from Centuries Past. ApJ, 612(1), 357–363. https://doi.org/10.1086/422419

Salvesen, G., Raymond, J. C., & Edgar, R. J. (2009). Shock Speed, Cosmic Ray Pressure, and Gas Temperature in the Cygnus Loop. ApJ, 702(1), 327–339. https://doi.org/10.1088/0004-637X/702/1/327

Sankrit, R., Raymond, J. C., Blair, W. P., Long, K. S., Williams, B. J., Borkowski, K. J., Patnaude, D. J., & Reynolds, S. P. (2016). Second Epoch Hubble Space Telescope Observations of Kepler's Supernova Remnant: The Proper Motions of Balmer Filaments. ApJ, 817(1), Article 36, 36. https://doi.org/10.3847/0004-637X/817/1/36

Sano, H., Yamane, Y., van Loon, J. T., Furuya, K., Fukui, Y., Alsaberi, R. Z. E., Bamba, A., Enokiya, R., Filipović, M. D., Indebetouw, R., Inoue, T., Kawamura, A., Lakićević, M., Law, C. J., Mizuno, N., Murase, T., Onishi, T., Park, S., Plucinsky, P. P., … Tachihara, K. (2023). ALMA Observations of Supernova Remnant N49 in the Large Magellanic Cloud. II. Non-LTE Analysis of Shock-heated Molecular Clouds. ApJ, 958(1), Article 53, 53. https://doi.org/10.3847/1538-4357/acffbe

Santra, R., Kale, R., Giacintucci, S., Markevitch, M., De Luca, F., Bourdin, H., Venturi, T., Dallacasa, D., Cassano, R., Brunetti, G., & Buch, K. D. (2024). A Deep uGMRT View of the Ultra-steep Spectrum Radio Halo in A521. ApJ, 962(1), Article 40, 40. https://doi.org/10.3847/1538-4357/ad1190

Sapienza, V., Miceli, M., Petruk, O., Bamba, A., Katsuda, S., Orlando, S., Bocchino, F., & DeLaney, T. (2024). Time Evolution of the Synchrotron X-Ray Emission in Kepler's Supernova Remnant: The Effects of Turbulence and Shock Velocity. ApJ, 973(2), Article 105, 105. https://doi.org/10.3847/1538-4357/ad6566

Shanahan, R., Stil, J. M., Anderson, L., Beuther, H., Goldsmith, P., Klessen, R. S., Rugel, M., & Soler, J. D. (2023). Turbulent Structure in Supernova Remnants G46.8-0.3 and G39.2-0.3 from THOR Polarimetry. ApJ, 957(2), Article 60, 60. https://doi.org/10.3847/1538-4357/acfe11

Shulevski, A., Brienza, M., Massaro, F., Morganti, R., Intema, H., Oosterloo, T., De Gasperin, F., Rajpurohit, K., Pasini, T., Kutkin, A., Vohl, D., Adams, E. A. K., Adebahr, B., Brüggen, M., Hess, K. M., Loose, M. G., Oostrum, L. C., & Ziemke, J. (2024). LOFAR discovery and wide-band characterisation of an ultra-steep spectrum AGN radio remnant associated with Abell 1318. A&A, 682, Article A171, A171. https://doi.org/10.1051/0004-6361/202346824

Sinitsyna, V. G., & Sinitsyna, V. Y. (2024). Particle acceleration test with Cas A multiwavelength emission. Astronomische Nachrichten, 345, Article e20240006, e20240006. https://doi.org/10.1002/asna.20240006

Smith, M. (2010, October). X-Ray and Radio Emission of the Galactic Supernova Remnant G7.7-3.7.

Soker, N. (2023). Supernovae in 2023 (review): breakthroughs by late observations. arXiv e-prints, Article arXiv:2311.17732, arXiv:2311.17732. https://doi.org/10.48550/arXiv.2311.17732

Stephenson, F. R., & Green, D. A. (2002). Historical supernovae and their remnants. Oxford University Press.

Tu, T.-Y., Chen, Y., Zhou, P., & Safi-Harb, S. (2024). Shock and Cosmic Ray Chemistry Associated with the Supernova Remnant W28. arXiv e-prints, Article arXiv:2403.13305, arXiv:2403.13305. https://doi.org/10.48550/arXiv.2403.13305

van den Bergh, S. (1978). A systematic search for galactic supernova remnants. ApJS, 38, 119–128. https://doi.org/10.1086/190549

Vasiliev, E. O., & Shchekinov, Y. A. (2024). Dust evolution in a supernova interacting with the ISM. MNRAS, 527(3), 8755–8767. https://doi.org/10.1093/mnras/stad3820

Vink, J. (2020). Physics and evolution of supernova remnants. Springer.

Vink, J., Patnaude, D. J., & Castro, D. (2022). The forward and reverse shock dynamics of cassiopeia a. The Astrophysical Journal, 929(1), 57.

Völk, H. J., Berezhko, E. G., & Ksenofontov, L. T. (2008). Internal dynamics and particle acceleration in Tycho's SNR. A&A, 483(2), 529–535. https://doi.org/10.1051/0004-6361:20079337

Williams, B. J., Blair, W. P., Blondin, J. M., Borkowski, K. J., Ghavamian, P., Long, K. S., Raymond, J. C., Reynolds, S. P., Rho, J., & Winkler, P. F. (2011). RCW 86: A Type Ia Supernova in a Wind-blown Bubble. ApJ, 741(2), Article 96, 96. https://doi.org/10.1088/0004-637X/741/2/96

Winkler, P. F., & Kirshner, R. P. (1985). Discovery of fast-moving oxygen filaments in Puppis A. ApJ, 299, 981–986. https://doi.org/10.1086/163764

Winkler, P. F., Tuttle, J. H., Kirshner, R. P., & Irwin, M. J. Kinematics of Oxygen-Rich Filaments in Puppis A (R. S. Roger & T. L. Landecker, Eds.). In: Iau colloq. 101: Supernova remnants and the interstellar medium (R. S. Roger & T. L. Landecker, Eds.). Ed. by Roger, R. S., & Landecker, T. L. 1988, January, 65.

Winkler, P. F., Long, K. S., & Blair, W. P. (2023). Supernova Remnants in the Irregular Galaxy NGC 4449. ApJ, 959(1), Article 62, 62. https://doi.org/10.3847/1538-4357/ad0237

Yang, H., & Chevalier, R. A. (2015). Evolution of the Crab Nebula in a Low Energy Supernova. ApJ, 806(2), Article 153, 153. https://doi.org/10.1088/0004-637X/806/2/153

Zhou, P., Vink, J., Li, G., & Domček, V. (2018). G7.7-3.7: A Young Supernova Remnant Probably Associated with the Guest Star in 386 CE (SN 386). ApJ, 865(1), Article L6, L6. https://doi.org/10.3847/2041-8213/aae07d

Zhou, X., Su, Y., Yang, J., Chen, Y., & Jiang, Z. (2024). Discovery of an old supernova remnant candidate through carbon monoxide line emission. A&A, 683, Article A107, A107. https://doi.org/10.1051/0004-6361/202348644

APPENDICES

Appendix A: G7.7-3.7 Radio Image Code (see Figure 4.1)

```
%matplotlib inline
import aplpy
import numpy
import astropy
import matplotlib
import matplotlib.pyplot as plt
from matplotlib.patches import Rectangle, Circle
from matplotlib.ticker import FuncFormatter
import os
import pyregion
import pyavm
import glob
from astropy.coordinates import SkyCoord
from astropy.coordinates import ICRS, Galactic, FK4, FK5
from astropy.coordinates import Angle, Latitude, Longitude
import astropy.units as u
from astropy.io import fits
```

```
# parameters for plots
plt.rcParams["font.serif"] = "Times"
plt.rcParams["font.size"] = 12
plt.rcParams['xtick.direction'] = 'in'
plt.rcParams['ytick.direction'] = 'in'
```

```
#to convert 4-D to 2-D fits file
def fix_aplpy_fits(aplpy_obj, dropaxis=2):
    """This removes the degenerated dimensions in APLpy 2.X...
    The input must be the object returned by aplpy.FITSFigure().
    `dropaxis` is the index where to start dropping the axis (by
                                        default it assumes the 3rd,4th
                                        place).
    """
    temp_wcs = aplpy_obj._wcs.dropaxis(dropaxis)
    temp_wcs = temp_wcs.dropaxis(dropaxis)
    aplpy_obj._wcs = temp_wcs
```

```
fig = plt.figure(figsize=(60,30))

f = aplpy.FITSFigure('/data/Radio_MeerKAT/
                                        img_1674190978_sdp_l0_1024ch_FRB20220330
                                        .ms_pcalmask-MFS-image.fits',
                                        dimensions=[0,1], slices=[1,-1])
fix_aplpy_fits(f)#convert 4-D to 2-D fits file
f.show_colorscale(vmin=0.000001,vmid=None,vmax=2e-04, stretch = 'linear
                                        ', aspect='auto',cmap='inferno')

f.recenter(274.375, -24.05, width=0.5, height=0.5)

f.axis_labels.show_x()
f.axis_labels.show_y()
f.add_colorbar()
f.colorbar.show()
f.colorbar.set_width(0.2)
```

```
f.colorbar.set_axis_label_text('Intensity (mJy/beam)')
f.colorbar.set_axis_label_font(size=12, weight='normal')
f.colorbar.set_font(size=12)
f.ticks.set_color('white')
f.ticks.set_length(5)
f.ticks.set_minor_frequency(5)
f.add_beam()
f.beam.show()
f.beam.set_color('white')

# Custom formatter to convert Jy/beam to mJy/beam
def colorbar_formatter(x, pos):
    return f'{x * 1e3:.3f}'
f.colorbar._colorbar.formatter = FuncFormatter(colorbar_formatter)
f.colorbar._colorbar.update_ticks()

f.savefig('Figures/G7_7_3_7_MeerKAT_Radio.png', dpi=600)
```

Appendix B: G7.7-3.7 Spectral Index Distribution Code (see Figure 4.2)

```
fig = plt.figure(figsize=(60, 30))

fSI = aplpy.FITSFigure('/data/Radio_MeerKAT/SN386_spectral_index_map.
                                    fits', dimensions=[0,1], slices=[1,
                                    -1])
#fix_aplpy_fits(fSI)#convert 4-D to 2-D fits file

fSI.recenter(274.377, -24.06,width=0.45, height=0.45)

fSI.show_colorscale(vmin=-3.0, vmid=None, vmax=0.5, stretch='linear',
                                    aspect='auto', cmap='plasma')
fSI.add_colorbar()
fSI.colorbar.show()
fSI.colorbar.set_width(0.2)
fSI.colorbar.set_axis_label_text('Spectral Index')
fSI.colorbar.set_axis_label_font(size=12, weight='normal')
fSI.axis_labels.set_font(size=12, weight='normal')
fSI.colorbar.set_font(size=12)
fSI.ticks.set_color('black')
fSI.ticks.set_length(5)
fSI.ticks.set_minor_frequency(5)
fSI.tick_labels.set_font(size=12)

fSI.savefig('Figures/G7.7_3.7_Spectral_Index.png', dpi=600)
plt.show()
```

Appendix C: Constraining the Age of G7.7-3.7 Code (see Figure 4.3)

```
import matplotlib.pyplot as plt
import numpy as np
import matplotlib.cm as cm

# Data: Age (in years), Shock Speed (in km/s), and Distance (kpc)
remnants_data = [
    ("G7.7-3.7", 1636, 5883, 4.4),
    ("Cas A", 335, 5800, 3.4),
    ("Tycho's SNR", 435, 3300, 2.85),
    ("Kepler's SNR", 4420, 1690, 5.1),
    ("Crab Nebula", 970, 1500, 2.0),
    ("Puppis A", 3700, 1500, 2.0),
    ("RCW 86", 1840, 7800, 2.5),
    ("G327.6+14.6", 1000, 5000, 2.2),
    ("W44", 3000, 45, 2.9),
    ("G266.2-1.2", 2400, 1000, 0.5),
    ("Cygnus Loop", 5000, 400, 0.57),
    ("G292.0+1.8", 3000, 1700, 6.0),
    ("G41.1-0.3", 1350, 1360, 8.0),
    ("G11.2-0.3", 1400, 1200, 4.4),
    ("G332.4-0.4", 2000, 1100, 4.7),
    ("G330.2+1.0", 1000, 9000, 5.0),
    ("G1.9+0.3", 150, 14000, 8.5),
    ("G310.6-1.6", 2500, 1000, 7.0),
    ("G350.1-0.3", 600, 6000, 4.5)
]

# Extracting ages, velocities, distances, and labels
ages = [item[1] for item in remnants_data]
velocities = [item[2] for item in remnants_data]
distances = [item[3] for item in remnants_data]
labels = [item[0] for item in remnants_data]

# Create figure and axis
fig, ax = plt.subplots(figsize=(9, 7))

# Normalize distances to use with colormap
norm = plt.Normalize(min(distances), max(distances))
cmap = cm.get_cmap('inferno')

# Plotting with different markers and color intensity representing
                                    distance
markers = ['*', 's', '^', 'D', 'o', '<', '>', 'p', 'v', 'h', 'P', 'x',
                                    'd', '+', '2', '1', '8', 'X', 'H',
                                    '_', '|']

for i, label in enumerate(labels):
    # Adding superscript index to the label using LaTeX format
    label_with_superscript = f'{label}$^{{{i+1}}}$'
    ax.scatter(ages[i], velocities[i], color=cmap(norm(distances[i])),
                                        label=label_with_superscript,
                                        marker=markers[i % len(markers)
                                        ], s=100)

# Adding labels and title
ax.set_xlabel("Age (years)", fontsize=12, weight='normal')
```

```
ax.set_ylabel("Shock Speed (km/s)", fontsize=12, weight='normal')
#ax.set_ylim([-500, 16000]) #setting y-max limit
ax.tick_params(axis='x', labelsize=12, width=1.5)
ax.tick_params(axis='y', labelsize=12, width=1.5)

# Add colorbar to show distance scale
sm = plt.cm.ScalarMappable(cmap=cmap, norm=norm)
sm.set_array([])  # Dummy for the color bar
cbar = plt.colorbar(sm, orientation='horizontal', pad=0, ax=ax,
                                    location='top', aspect=40)
cbar.set_label('Distance (kpc)', fontsize=12, weight='normal')
cbar.ax.tick_params(labelsize=12, width=1.5)

# Adjust layout and add legend
ax.legend(bbox_to_anchor=(0.78, 1.01), loc='upper left', prop={'size':
                                    10.4, 'weight': 'normal'})
plt.tight_layout()

# Save the figure
save_path = '/Figures/SNRs_velocity_age_distribution_map.png'
plt.savefig(save_path, dpi=600)

# Show plot
plt.show()
```

Appendix D: X-ray Emissions in G7.7-3.7 Code (see Figure 4.4)

```
fig = plt.figure(figsize=(60,30))

fx = aplpy.FITSFigure('/data/X-Ray/P0840940101PNS003IMAGE_8000.FIT',
                                    dimensions=[0,1], slices=[1,-1])

fx.show_colorscale(vmin=10,vmid=None,vmax=60, stretch = 'linear',
                                    aspect='auto',cmap='jet')

fx.recenter(274.375, -24.1, width=0.5,height=0.5)

fx.add_colorbar()
fx.colorbar.show()
fx.colorbar.set_width(0.2)
fx.colorbar.set_axis_label_text('Counts')
fx.colorbar.set_axis_label_font(size=12, weight='normal')
fx.colorbar.set_font(size=12, weight='normal')
fx.ticks.set_color('white')
fx.ticks.set_length(5)
fx.ticks.set_minor_frequency(5)
fx.tick_labels.set_font(size=12)

fx.savefig('Figures/G7_7_3_7_XMM_X-ray.png')
```

Appendix E: G7.7-3.7 Optical Emitting Region Cutout Code (Figure 4.6)

```
Ha='/data/Optical/diff_ha_fluxed.fits'
OIII='/data/Optical/diff_o3_fluxed.fits'
SII= '/data/Optical/diff_s2_fluxed.fits'

# create rgb cube from fits files
aplpy.make_rgb_cube([Ha, OIII, SII], 'sum.fits')

# create rgb image
aplpy.make_rgb_image('sum.fits', 'sum.png',
                     vmin_r=-1e-4, vmax_r=3e-4,
                     vmin_g=-1e-5, vmax_g=3e-5,
                     vmin_b=-1e-5, vmax_b=6e-5,
                     stretch_r='linear',stretch_g='linear', stretch_b=
                                                          'linear')
fOrgb = aplpy.FITSFigure('sum_2d.fits')
fOrgb.show_rgb('sum.png')

# Convert world coordinates to pixel coordinates for Filaments A & B
x_A, y_A = fs2.world2pixel(274.37, -24.217)
x_B, y_B = fs2.world2pixel(274.31, -24.180)

# Adding the text box for both filaments
plt.annotate('Filament A', xy=(x_A, y_A), xycoords='data',
             fontsize=12, color='black', weight='bold', bbox=dict(
                                                  facecolor='white',
                                                  edgecolor='none',
                                                  alpha=1))
plt.annotate('Filament B', xy=(x_B, y_B), xycoords='data',
             fontsize=12, color='black', weight='bold', bbox=dict(
                                                  facecolor='white',
                                                  edgecolor='none',
                                                  alpha=1))

fOrgb.axis_labels.show_x()
fOrgb.axis_labels.show_y()
fOrgb.ticks.set_color('white')
fOrgb.ticks.set_length(5)
fOrgb.ticks.set_minor_frequency(5)
fOrgb.tick_labels.set_font(size=12)
fOrgb.axis_labels.set_font(size=12, weight='normal')

fOrgb.savefig('Figures/G7.7_3.7_Optical_RGB_linear_scale.png')
```

Appendix F: Combined Radio, X-ray and Optical Observation for G7.7-3.7 Code (see Figure 4.7)

```
fig = plt.figure(figsize=(10,10))

f = aplpy.FITSFigure('/data/Radio_MeerKAT/
                                    img_1674190978_sdp_l0_1024ch_FRB20220330
                                    .ms_pcalmask-MFS-image.fits',
                                    dimensions=[0,1], slices=[1,-1],
                                    figure=fig)
fix_aplpy_fits(f)
f.show_colorscale(vmin=0.000001, vmid=None, vmax=2e-04, stretch='linear
                                    ', aspect='auto', cmap='inferno')
#X-ray contours
f.show_contour('/data/X-Ray/P0840940101PNS003IMAGE_8000.FIT', levels=[
                                    20, 40, 60, 80, 100, 120, 140],
                                    colors='cyan', linewidths=2)

f.recenter(274.43, -24.00, width=0.55, height=0.55)

f.axis_labels.show_x()
f.axis_labels.show_y()
f.add_colorbar()
f.colorbar.show()
f.colorbar.set_width(0.2)
f.colorbar.set_axis_label_text('Intensity (mJy/beam)')
f.colorbar.set_axis_label_font(size=12, weight='normal')
f.colorbar.set_font(size=12)
f.ticks.set_color('white')
f.ticks.set_length(5)
f.ticks.set_minor_frequency(5)
f.tick_labels.set_font(size=12)
f.axis_labels.set_font(size=12, weight='normal')

# Custom formatter to convert Jy/beam to mJy/beam
def colorbar_formatter(x, pos):
    return f'{x * 1e3:.3f}'

f.colorbar._colorbar.formatter = FuncFormatter(colorbar_formatter)
f.colorbar._colorbar.update_ticks()

# Coordinates in degrees for Optical region
x_start, y_start = 274.39166667, -24.16666667
x_end, y_end = 274.26666667, -24.225

# Convert world coordinates to pixel coordinates
x_start_pixel, y_start_pixel = f.world2pixel(x_start, y_start)
x_end_pixel, y_end_pixel = f.world2pixel(x_end, y_end)

# Draw a rectangle on the plot
rect = Rectangle((x_start_pixel, y_start_pixel), x_end_pixel -
                                    x_start_pixel, y_end_pixel -
                                    y_start_pixel, linewidth=3,
                                    edgecolor='blue', facecolor='none',
                                     linestyle='dotted')
f.ax.add_patch(rect)

# Load the optical subplot
```

```
fha = aplpy.FITSFigure('/data/Optical/14new_diff_ha_fluxed.fits',
                                    figure=fig, subplot=[0.127, 0.627,
                                    0.45, 0.25])
fha.show_colorscale(vmin=0, vmax=3e-04, stretch='linear', aspect='auto'
                                    , cmap='jet')
fha.ticks.hide()
fha.tick_labels.hide()
fha.axis_labels.hide()

# Add lines connecting the rectangle to the subplot
line_color = 'blue'
line_style = 'dotted'
line_width = 3

# Get the rectangle top corners in pixel coordinates
rect_top_left = (x_start_pixel, y_start_pixel)
rect_top_right = (x_end_pixel, y_start_pixel)

# Get the bottom corners of the subplot in figure coordinates
fha_ax = fha.ax
subplot_bottom_left = fha_ax.transAxes.transform((0, 0))
subplot_bottom_right = fha_ax.transAxes.transform((1, 0))

# Convert subplot figure coordinates to display coordinates
subplot_bottom_left_display = fig.transFigure.inverted().transform(
                                    subplot_bottom_left)
subplot_bottom_right_display = fig.transFigure.inverted().transform(
                                    subplot_bottom_right)

# Convert display coordinates to data coordinates of the main plot
subplot_bottom_left_data = f.ax.transData.inverted().transform(fig.
                                    transFigure.transform(
                                    subplot_bottom_left_display))
subplot_bottom_right_data = f.ax.transData.inverted().transform(fig.
                                    transFigure.transform(
                                    subplot_bottom_right_display))

# Plot lines
f.ax.plot([rect_top_left[0], subplot_bottom_left_data[0]],
          [rect_top_left[1], subplot_bottom_left_data[1]],
          color=line_color, linestyle=line_style, linewidth=line_width)

f.ax.plot([rect_top_right[0], subplot_bottom_right_data[0]],
          [rect_top_right[1], subplot_bottom_right_data[1]],
          color=line_color, linestyle=line_style, linewidth=line_width)

# Convert world coordinates to pixel coordinates for Filaments A & B
                                    within f2
x_A_fha, y_A_fha = fha.world2pixel(274.365, -24.219)
x_B_fha, y_B_fha = fha.world2pixel(274.31, -24.179)

# Adding the text boxes for both filaments
fha.ax.annotate('Filament A', xy=(x_A_fha, y_A_fha), xycoords='data',
               fontsize=12, color='black', weight='bold', bbox=dict(
                                                   facecolor='white',
                                                   edgecolor='none',
                                                   alpha=1))
fha.ax.annotate('Filament B', xy=(x_B_fha, y_B_fha), xycoords='data',
```

```
                fontsize=12, color='black', weight='bold', bbox=dict(
                                                    facecolor='white',
                                                    edgecolor='none',
                                                    alpha=1))

fig.canvas.draw()
plt.show()

f.savefig('Figures/G7.7_3.7_Mosaic1.png', dpi=600)
```

Appendix G: Poster Presented in XXXII IAU General Assembly 2024

MeerKAT-Based Multi-Wavelength Study of Supernova Remnant SN386 (G7.7-3.7)

Patrick N. Mwaniki [1] James O. Chibueze [2] Dismas S. Wamalwa [1]

[1]Department of Physical Sciences, Meru University of Science and Technology, Meru, Kenya. [2]Department of Mathematical Sciences, University of South Africa, South Africa.

Abstract

MeerKAT observations revealed G7.7-3.7 as an almost circular structure with filamentary structures. The western boundary exhibits a strong bright blowout, while the southern perimeter showcases extended bright filaments with feather-like structures, seemingly disconnected from the western blowout. Moreover, the eastern region presents a faint blowout with a centralized bright point source, while faint elongated filaments traverse the northwest, linking the eastern point source and the western blowout. Spectral index analysis indicates a steep spectrum, suggesting a synchrotron emission. Furthermore, the multi-wavelength investigation unveils an intriguing enigma within the southern radio-bright blowout. This blowout exhibits a convergence of features, including a radio-bright blowout, a prominent X-ray arc, and two faint optical filaments aligned with the X-ray bright arc. The bright radio blowouts result from weakened magnetic fields and heightened particle density in the blowout. Also, the supernova of G7.7-3.7 occurred in an environment of varying densities of ISM. Consequently, this environment facilitates X-ray emission and the formation of faint optical filaments due to collisions with the ISM.

Introduction

Very Large Array (VLA) and Molonglo Observatory Synthesis Telescope (MOST) observation of G7.7-3.7 revealed a shell with bright synchrotron emissions in the west, south and east with faint ones filling north-west [3, 4]. MeerKAT observation at 1335 MHz and 10″ resolves this shell into faint thin filaments with blowouts in the west, south and east [1]. However, the origin of the observed blowouts remains an unresolved puzzle. To approach this puzzle, we observed G7.7-3.7 with the MeerKAT telescope at 1284 MHz with a beam of 5″.7 and combine with existing X-ray and optical observations.

Observation

G7.7-3.7 was observed with 62 antennas of the MeerKAT array in L-band. The OXKAT pipeline, semi-automated MeerKAT data analysis pipeline, was used to reduce the data. Spectral index map, fig 2, was generated using CASA task immath. We retrieved the most recent X-ray and optical data from XMM-Newton Science Archive and 2.5 m Isaac Newton Telescope (INT) in La Palma Spain respectively to combine them with radio data.

Results

G7.7-3.7 Radio Image

MeerKAT image of G7.7-3.7 (fig 1) with a circular beam of 5″.7 at 1284 MHz presents an almost circular structure with filamentary structures spanning an average diameter of ∼27′. G7.7-3.7 has a strong bright blowout in the western boundary and extended bright filament in the southern perimeter with feather-like filaments seemingly disconnected from the western bright blowout. In the eastern, it has a faint blowout with a bright point source at the center. Northwest is occupied by very faint elongated filaments connecting the eastern point source and the western bright blowout. The resolved filamentary structure of G7.7-3.7 with blowouts along its western, southern, and eastern boundaries looks like its outer perimeter consists of mainly mass outflows [1]. The non-uniform mass outflow of the progenitor star results in the non-uniform particle density distribution of the remnant.

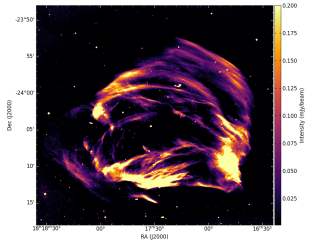

Figure 1. MeerKAT image of G7.7-3.7 with 5″.7 at 1284 MHz.

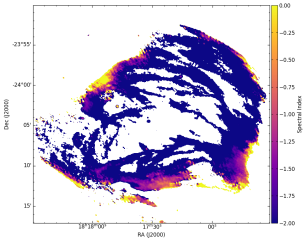

Figure 2. The distribution of spectral index of G7.7-3.7.

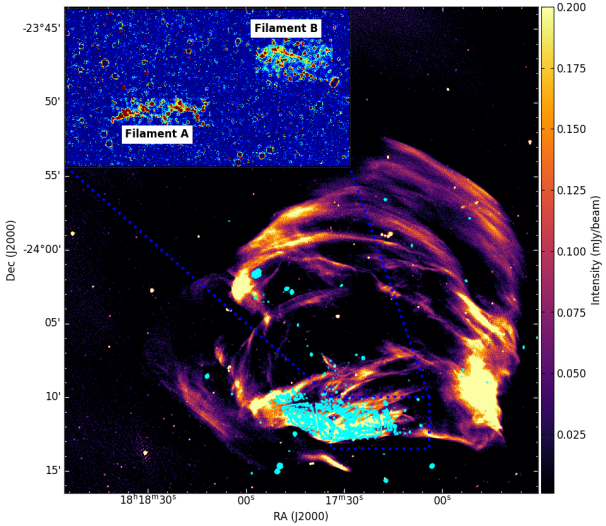

Figure 3. A mosaiced MeerKAT radio image of G7.7-3.7 (inferno). Cyan displays the XMM-Newton contours of G7.7-3.7 (see fig. 1 in [5]). The dashed blue rectangle displays a region with the INT detected faint optical emission whose H α + [N II] image is projected at the top left corner (see fig. 1 & 2 in [2]).

G7.7-3.7 Spectral Index Distribution

Spectral index distribution map of G7.7-3.7 (fig 2) reveals a fluctuating spectrum suggesting a synchrotron emission. Brighter blowouts have less steep spectral indices ranging ∼ -0.6 to ∼ -1.2, while the dimmer and more diffuse filaments show very steep spectral indices, ∼ -2. Brighter radio blowouts, characterized by relatively less steep indices ranging ∼ -0.6 to ∼ -1.2, could have shock acceleration processes accelerating particles to higher energies to emit strong synchrotron emission.

On the other hand, in the dim and diffuse filaments with very steep spectral indices, ∼ -2, the observed steepening may be indicative of particles reaching the cut-off energy before reaching the higher energies and/or having low particle densities required to emit bright synchrotron radiation.

G7.7-3.7 Multi-Wavelength Nature

The multi-wavelength structure (fig 3) revealed that G7.7-3.7 has a non-uniform distribution of X-ray emission with the only bright arc-like feature in the southern radio blowout and the interior filled with diffuse X-ray emissions. The optical observation of G7.7-3.7 in Hα + [N II], [O III], and marginally in [S II] narrow-band showed two faint filaments aligned with the X-ray south arc-like feature in the southern radio blowout. It is likely that G7.7-3.7 is expanding in a low-density environment and colliding with ISMs [5]. The low-density ISM could result in diffuse and faint X-ray emissions in the interior of G7.7-3.7. The non-uniform ISM density distribution could result in a not-so-spherical radio structure. The presence of a high-density wall could result in intense X-ray emissions in the south. The composition of this high-density wall with circumstellar materials from the progenitor star could result in the formation of an optical filament in the south and intense X-ray emission.

Conclusion

MeerKAT radio observations of G7.7-3.7 with 5″.7 at 1284 MHz reveal a strong bright blowout in the western boundary, southern and eastern. The spectral index distribution map of G7.7-3.7 revealed a fluctuating spectrum suggesting a non-thermal synchrotron emission. The radio blowouts originate from the non-uniform mass outflow from the localized high-density population of the shock-accelerated particles and the weakening of magnetic fields along its perimeter. G7.7-3.7 multi-wavelength study revealed captivating attention in the southern radio blowout. This blowout exhibits a coincidence of features, including a radio blowout, a bright X-ray arc, and two faint optical filaments aligned with the X-ray arc. G7.7-3.7 is likely expanding in a low-density environment and colliding with ISM. The collision of the shock front with ISM results in X-ray emission while with the circumstellar materials results in faint optical filaments.

Acknowledgement

This article makes use of the MeerKAT data. The MeerKAT telescope is operated by the South African Radio Astronomy Observatory (SARAO), facility of the National Research Foundation, an agency of the Department of Science and Innovation (DSI). We are grateful to XMM-Newton and Isaac Newton Telescope (INT) for the data available for G7.7-3.7.

References

[1] W. D. Cotton, R. Kothes, F. Camilo, P. Chandra, S. Buchner, and M. Nyamai.
MeerKAT 1.3 GHz Observations of Supernova Remnants.
, 270(2):21, February 2024.

[2] V. Domček, J. V. Hernández Santisteban, A. Chiotellis, P. Boumis, J. Vink, S. Akras, D. Souropanis, P. Zhou, and A. de Burgos.
Detection of optical emission from the supernova remnant G7.7-3.7.
, 526(1):1112–1121, November 2023.

[3] G. M. Dubner, E. B. Giacani, W. M. Goss, D. A. Moffett, and M. Holdaway.
VLA Observations of Nine Galactic Supernova Remnants.
, 111:1304, March 1996.

[4] D. K. Milne, R. S. Roger, M. J. Kesteven, R. F. Haynes, K. J. Wellington, and R. T. Stewart.
G 7.7 - 3.7 - a supernova remnant with a high degree of radio polarization.
, 223:487–495, December 1986.

[5] Ping Zhou, Jacco Vink, Geng Li, and Vladimir Domček.
G7.7-3.7: A Young Supernova Remnant Probably Associated with the Guest Star in 386 CE (SN 386).
, 865(1):L6, September 2018.

Appendix H: Publication

New Astronomy 117 (2025) 102370

Contents lists available at ScienceDirect

New Astronomy

journal homepage: www.elsevier.com/locate/newast

MeerKAT-based multi-wavelength study of supernova remnant G7.7-3.7 (SN386?)

Patrick N. Mwaniki [a,*], James O. Chibueze [b], Dismas S. Wamalwa [a]

[a] Department of Physical Sciences (Physics), Meru University of Science and Technology, P.O. Box 972, 60200, Meru, Kenya
[b] Department of Mathematical Sciences, University of South Africa, Cnr Christian de Wet Rd and Pioneer Avenue, Florida Park, 1709, Roodepoort, South Africa

ARTICLE INFO

Keywords:
G7.7-3.7
Supernovae
Supernova remnants
Spectral index
Interstellar medium

ABSTRACT

We investigated the structural characteristics of G7.7-3.7 at a higher resolution of 1284 MHz. MeerKAT observations revealed that G7.7-3.7 had an asymmetric spherical structure with filamentary features and various blowouts. The western boundary showed a strong bright blowout, while the southern perimeter showcased extended bright filaments with feather-like structures, which seemed disconnected from the western blowout. Moreover, the eastern region exhibited a blowout centered around a bright point source, with faint, elongated filaments extending north-west. These filaments connected the eastern point source to the western blowout, creating a uniform outward progression. Spectral index analysis indicated a steep spectrum (α ranged ~ 0 to ~ -3), suggesting a combination of synchrotron and a few traces of thermal emissions concentrated at the edges of bright blowouts. Analysis of MeerKAT and VLA data revealed that G7.7-3.7 had expanded by 9 ± 0.45 arcsec over a period of 31.907 years, corresponding to an expansion rate of 0.282 ± 0.014 arcsec yr^{-1}. This expansion indicated a shock speed of 5883 ± 294 km s^{-1} and an age of 1636 ± 115 years. This age fits with the supernova explosion event of 386 CE and the MeerKAT observed data in 2023. The multi-wavelength investigation unveiled a distinctive structure within the southern radio blowout, encompassing a bright radio blowout, a prominent X-ray arc, and two faint optical filaments aligned with the X-ray bright arc. We attributed the bright radio blowouts to inhomogeneous mass outflow from shock-accelerated particles and the weakening of magnetic fields along its perimeter. Traces of thermal emissions, especially along the edges of blowouts, were likely due to shock-heated gas, which intensified in the southern region amid high-density Interstellar Medium (ISM). Therefore, these results supported a scenario in which the progenitor supernova of G7.7-3.7 exploded within ISM of varying density, generating the observed X-ray emissions and faint optical filaments. Our findings provided valuable insights into the dynamics and evolution of supernova remnants.

1. Introduction

Supernova remnants (SNRs) are the remnants of massive stars that have undergone explosive supernova events initiated by the catastrophic gravitational collapse (Dubner, 2008; Vasiliev and Shchekinov, 2024; Michailidis et al., 2024; Hirashima et al., 2023). These events, among the most energetic in the universe, Zhou et al. (2018), leave behind expanding shells of gas and dust that can be observed across multiple wavelengths (Dubner and Giacani, 2015). The study of SNRs provides valuable insights into the life cycles of stars, the mechanisms of supernova explosions, and their impact on the surrounding interstellar medium (ISM) (Dubner et al., 1996; Green, 2015; Vink, 2020; Leahy et al., 2022; Dubner and Giacani, 2015; Zhou et al., 2024). SNRs also offer a unique opportunity to investigate the acceleration of cosmic rays, Vink (2020), Domček et al. (2023), and the properties of magnetic fields in the Milky Way galaxy (Dubner et al., 1996; Dubner and Giacani, 2015).

One such SNR of interest is G7.7-3.7, which is located within the Nan-Dou asterism (Stephenson and Green, 2002). G7.7-3.7 was initially documented as a radio source in early catalogs during the 1960s, bearing the catalog number PKS 1814-24 (Gardner et al., 1969). This subtle, diffuse radio source is located at coordinates $\sim$ ($18^h17^m25^s$, -24 °04′) (B1950) (Dubner et al., 1996; Green, 2014, 2019). It was initially recognized as a supernova remnant (SNR) by Milne and Dickel (1974b). In recent studies, Zhou et al. (2018) proposed that G7.7-3.7 could potentially be linked to the supernova event of 386 CE (SN 386) through examination of historical record matching. Furthermore, they suggested that G7.7-3.7 might represent one of the rare instances of historical SNRs resulting from a supernova with extremely low

* Corresponding author.
E-mail address: patonjo522@gmail.com (P.N. Mwaniki).

https://doi.org/10.1016/j.newast.2025.102370
Received 12 November 2024; Received in revised form 24 January 2025; Accepted 31 January 2025
Available online 8 February 2025